

SURFACE BRIGHTNESS PROFILES OF GALACTIC GLOBULAR CLUSTERS FROM HUBBLE SPACE TELESCOPE IMAGES

EVA NOYOLA KARL GEBHARDT
 Astronomy Department, University of Texas at Austin, Austin, TX 78712
Draft version February 5, 2008

ABSTRACT

Hubble Space Telescope allows us to study the central surface brightness profiles for globular clusters at unprecedented detail. We have mined the *HST* archives to obtain 38 WFPC2 images of galactic globular clusters with adequate exposure times and filters, which we use to measure their central structure. We outline a reliable method to obtain surface brightness profiles from integrated light that we test on an extensive set of simulated images. Most clusters have central surface brightness about 0.5 mag brighter than previous measurements made from ground-based data, with the largest differences around 2 magnitudes. Including the uncertainties in the slope estimates, the surface brightness slope distribution is consistent with half of the sample having flat cores and the remaining half showing a gradual decline from 0 to -0.8 ($d\log\Sigma/d\log r$). We deproject the surface brightness profiles in a non-parametric way to obtain luminosity density profiles. The distribution of luminosity density logarithmic slopes show similar features with half of the sample between -0.4 and -1.8 . These results are in contrast to our theoretical bias that the central regions of globular clusters are either isothermal (i.e. flat central profiles) or very steep (i.e. luminosity density slope ~ -1.6) for core-collapse clusters. With only 50% of our sample having central profiles consistent with isothermal cores, King models appear to poorly represent most globular clusters in their cores.

Subject headings: globular clusters:general, stellar dynamics

1. INTRODUCTION

1.1. Surface Brightness Profiles

Globular clusters (GC) are nearby isolated and relaxed systems, which makes them good laboratories to study stellar dynamical processes. As a first step for any dynamical model, we require a measure of the surface brightness profile. Dynamical processes such as core-collapse, influence of a central black hole, and the physics of the initial collapse (Bahcall & Wolf 1977; Cohn 1980; Gnedin et al. 1999) will influence the central surface brightness profile, while tidal influences and evaporation leave noticeable effects at larger radius. The standard view is to assume that the central regions are isothermal and the outer regions are tidally truncated by the galaxy. King models (King 1966; Meylan & Heggie 1997) provide a theoretical base for their study. However $\sim 20\%$ of the galactic globular clusters show deviations from King models by having steeper central surface brightness profiles (Djorgovski 1995). These clusters have historically been called post core-collapse since this steepening of the central profile is the expected behavior during core-collapse (Cohn 1980). Given the large amount of data collected from the Hubble Space Telescope (*HST*), our goal here is to characterize the central profile in a non-parametric way, thereby testing whether the cores are in fact isothermal or consistent with the expected post core-collapse morphology.

The surface brightness (SB) profile provides a fairly simple way to obtain the mass distribution through deprojection; therefore, reliable SB profiles of any stellar system are necessary for detailed dynamical modeling. In the case of globular clusters, most dynamical studies use parameters such as central surface brightness and half light radius obtained from King model fits to the observed SB. Trager et al. (1995) provide the most complete catalog for GC radial profiles. This catalog contains profiles constructed from ground-based im-

ages using a combination of star counts and integrated light; they also provide King model fits to determine core radius, concentration and central surface brightness. It is worth noting that the concentration is the only parameter they obtain directly from the King model fit; the other two parameters are obtained from a Chebychev polynomial fit to the photometric points. They report uncertainties from a variety of sources, some are relevant to the outer part of the profiles like sky brightness determination, while others are particularly important for the inner parts of the profile such as center determination and crowding correction for star counts. They report a seeing of 2–3 arcsec for the observations. While this catalog is extremely useful for analyzing the outer parts of the SB profile, it is necessary to update the data for the innermost regions using *HST*'s resolution. Another study using ground-based images in the U filter is performed by Lugger et al. (1995) on 15 core-collapse clusters. They fit pure power-law and modified power-law (which allows the existence of a core) to the central surface brightness of these objects. They find that nine have unresolved cores, three have marginally resolved cores, and three have clearly resolved cores. The average slope of the power-law fits is ~ -0.8 . They conclude that clusters in their sample, with the exception of one object (NGC 6752), have cores

consistent with expectations for a post-collapse bounce.

Some specific clusters have been studied in more detail. Particularly, M15 has been the subject of many studies trying to obtain a reliable radial profile (either in light or in star counts) near the center. Lauer et al. (1991), using WFPC, claimed to see a core of $1.1''$; later analysis by Guhathakurta et al. (1996) using WFPC2 found a steep cusp into the smallest resolution element with a slope of -0.7 . This result is similar to that of Sosin & King (1997) using FOC images. Our results agree with those of Guhathakurta et al. (1996), as discussed in Section. 4.3.3. Less detailed studies have obtained SB profiles from *HST* images for M30

(Yanny et al. 1994; Sosin 1997), NGC 6397 (King et al. 1995) and NGC 6752 (Ferraro et al. 2003).

In this paper we present surface brightness profiles from *HST* images for 38 Galactic globular clusters. In section 2 we describe analysis of our simulated datasets that allow us to optimize the extraction of the surface brightness profile. In section 3 we describe the data acquisition, estimation of the surface brightness profiles and their uncertainties. In section 4 we discuss the results focusing on the central slope values.

1.2. *Effects of Dynamical Evolution on the Surface Brightness Profile*

Core collapse is thought to be the process responsible for why radial profiles deviate from King profiles, therefore, we briefly discuss it. Core collapse occurs when weak gravitational interactions between stars drive the central density of the cluster to larger values while the core radius decreases. This process can be separated in two stages. First, close encounters drive stars to the halo of the cluster eventually causing them to evaporate, and the core shrinks due to energy conservation. This process alone drives core-collapse over long timescales. A second process, the energy exchange between the outer halo and the inner core, accelerates the timescale for core collapse. Mass segregation from two-body relaxation drives energy from the core to the outer halo, and increases the velocity dispersion in the core while it contracts.

A number of simulations have been carried out to provide a detailed description of core-collapse using both N-body codes (Makino 1996) and numerical integrations of the multi mass Fokker-Planck equation (Breedon et al. 1994; Murphy et al. 1990; Chernoff & Weinberg 1990; Cohn et al. 1989). They all show that the projected density will have a shallower central slope for the lower mass stars compared with the high mass stars, although the precise slope for the visible stars depends on initial conditions. When the presence of binary systems is included in the simulations, it is seen that they have important effects on core collapse evolution. The presence of primordial binaries has the effect of delaying core collapse, but even if there are no primordial binaries present in the cluster core, hard binaries are formed by three body encounters once core collapse begins. These binaries act as a energy source for the core, cooling it. This in turn reverses the contraction process and produces an expansion. Eventually, the core contracts again and the whole process happens periodically, which results in what is known as “gravothermal oscillations”. At this stage, the cluster successively goes in and out of core collapse. It is shown in these simulations that core-collapse occurs on a very short time scale. The core quickly re-expands and spends a longer time in a state similar to pre-collapse between the successive contractions, but with a much smaller core with radius of a few percent the half-mass radius.

(Cohn et al. 1989) predict a central slope of the luminosity density due to core-collapse of about -1.7 for turn-off stars, including effects from the present mass function with remnants. However, this slope obviously depends on the mass function, the stage of core-collapse, and the spatial resolution of the measurements. For instance, Meylan (1988) measure a non-zero slope for 47Tuc whereas we find a nearly zero with our improved spatial resolution (as was found by Trager et al. (1995)). Another case is NGC6397, where (Lugger et al. 1995) measure a steep cusp from data at large radii, however at small radii they find a core (they infer that we are seeing NGC6397 in an expanded-core post collapse state). Thus, in this case, where you define the radii over which the slope is

measured is crucial. Our goal in this paper is to measure the slope at the smallest radii possible in order to make the most systematic measurement possible to compare with theoretical results. In this way, we are not subject to the particulars of the theoretical bias for what you assume the surface brightness profile should have.

Dull et al. (1997) compare Fokker-Planck simulations to the observed surface brightness and velocity dispersion profiles for M15. They conclude that these profiles are consistent with an intermediate state between core-collapse and re-expansion. In a state of complete re-expansion, the cluster would show a $\sim 1.2''$ or larger core, which should be observable. If we assume all clusters with unresolved cores ($\sim 20\%$ of galactic clusters) are in a similar state and we take into account the fact that during gravothermal oscillations the core spends a very short time in the collapse state, then we are catching a very high number of galactic clusters in the act of core-collapse.

Another dynamical scenario that has been explored as part of the evolution of globular clusters is the possible presence of a central black hole. Silk & Arons (1975) suggested that central X-ray sources in clusters could be produced by gas fed into a $100\text{--}1000M_{\odot}$ black hole. Bahcall & Wolf (1977) calculated the effect on the stellar distribution for a cluster if a black hole is present in its center. They predict the formation of a cusp near the center with a logarithmic slope of ~ -1.75 for the most massive stars in the 3-dimensional density, while the limiting slope for least massive stars is ~ -1.5 . The predicted slope of the surface brightness distribution is very close to that predicted for core-collapse for the dominant stellar components in the core, but the variation with mass is less dramatic than for the core-collapse case. Most observable mass groups would have a logarithmic SB slope ~ -0.7 (Sosin & King 1997). Baumgardt et al. (2004) perform extensive simulations of star clusters containing an intermediate mass black hole (IMBH). They find that the presence of the black hole induces the formation of a cusp whose 3-dimensional density profile has a ~ -1.55 slope. In projection the slope of the cusp is much shallower, yet different than zero. Recently, there have been two claims for the presence of a medium size black hole at the center of two globular clusters. One is for M15 (Gebhardt et al. 2000; Gerssen et al. 2002, 2003) and the other one is for the giant globular cluster G1 in M31 (Gebhardt et al. 2002). Although this is still a very controversial subject (Baumgardt et al. 2003b,a), it is crucial to be able to differentiate between the two possible dynamical states (i.e. core-collapse vs. intermediate mass black hole). Having reliable SB profiles near the center of GCs will be a key part of future dynamical modeling.

1.3. *Non-parametric Models*

Here, we concentrate on the differences between parametric and non-parametric techniques for estimating the surface brightness. The way in which we characterize light profiles has important consequences for dynamical analysis. The advantage of using King models lies in the fact that they provide a smooth profile even for sparsely sampled data, and that they have an analytical deprojection. However, the quality of the data is now good enough that it is not necessary to use a parametric profile. Furthermore, small differences or biases between the parametric fits and the data will be greatly amplified during deprojection, causing the luminosity density to be possibly poorly represented by King models. Parametric fits have a side effect of underestimating the confidence in-

tervals for three dimensional distributions, since the range of possible solutions is always larger for non-parametric analysis than for a parametric one. The draw-back of not forcing a functional form to the distribution is that the data always have some amount of noise. Deprojection involves a derivative of the surface brightness profile; therefore, any amount of noise will be greatly amplified during the deprojection. Thus, non-parametric algorithms require some degree of smoothing, and the reliability of the result depends on the technique and the amount of smoothing used. Ultimately, there is a problem of assessing whether the fluctuations in the data are real or not. This is particularly important when the focus of the study is the inner parts of globular clusters. In this work, we use a non-parametric approach to analyze our data, similar to that used for galaxies in Gebhardt et al. (1996).

2. SIMULATIONS

There have been a variety of techniques used in the literature to measure radial profiles for globular clusters, both with star counts and integrated light. We performed extensive simulations in order to test the reliability of different methods for obtaining accurate surface brightness profiles, which we describe below.

The two most complete studies to date base results on star counts and both correct for completeness. Sosin & King (1997) use artificial star tests in order to obtain a SB profile for M15. They add synthetic stars over their image of M15 and measure the recovery rate of their photometry software. A problem in this case is that it is hard to know the effect of the underlying stellar distribution on the results, since the true stellar distribution is not known. Guhathakurta et al. (1996) perform simulations over a blank image, controlling all the input variables. They compare the photometry of input and output stars one by one, calculate a completeness factor for the number of stars in a given annulus and construct the SB profile from star counts using those correction factors. This is very reliable but it does not test for degeneracy that could arise from different underlying profiles yielding the same final result. Since our goal is to provide a general prescription by studying the full range of profile slopes, our method should not depend on the type of profile for each cluster (i.e. cusp vs. core). We perform simulations over blank images, thus having control over the input parameters such as the stellar profile, luminosity function and total number of stars. Below we outline each step. We argue that using integrated light is superior for measuring an unbiased SB profile (compared to star counts) if the cluster contains a large enough number of stars.

2.1. Image Construction

Our goal is to create images that resemble the PC chip as closely as possible. The first step toward creating images is to produce an input list of stars. We start with a luminosity function for M5 (Jimenez & Padoan 1998) and a desired surface brightness profile. The effect of mass segregation is not included in these simulations. From the functional form of these two profiles, we construct a probability distribution for a star having a certain magnitude (from the luminosity function) and radial distribution (from the surface brightness profile). Stars are generated randomly around a given center from those probability distributions. By performing star counts in magnitude bins we confirm that our resulting star list represents the supplied luminosity function. The same test is performed in radial bins for surface brightness. With

this method, we create various master lists of stars of a given surface brightness profile. Results with fainter and brighter versions of the luminosity function are discussed below. We use five different power-law profiles $\Sigma(r) = r^{-\beta}$, with β of 0.1, 0.3, 0.5, 0.7 and 1.0 as the supplied functions for the surface brightness. We also create images for a King profile with a core radii of 90 pixels. The images have 200,000, 50,000, 10,000, and 1,500 input stars within a 200 pixel radius (20'' for WFPC2 pixel scale). Five individual realizations are created for each pair of input number of stars and profile shape with the goal of performing statistical analysis.

The images are created using the DAOPHOT (Stetson 1987) routine "ADDSTAR". For a base image, we use an actual WFPC2 image containing very few stars that are cleanly subtracted. This process results in a realistic background including cosmic rays and bad pixels. The routine adds Poisson noise and read out noise as well. The supplied point spread function (PSF) is constructed from the base *HST* image. We do not include spatial variation of the PSF since its relevance varies a lot for each real dataset. The PSF radius defined for DAOPHOT when building these images is 9 pixels.

2.2. Center Determination

Having a good estimate of the center position of a cluster is crucial to obtain an accurate surface brightness profile. Using the wrong center typically produces a shallower inner profile. We design a technique to measure the center that assumes the cluster is symmetric. A guess center and a radius from that center are chosen. The resulting circle is divided in eight segments where we count stars and then we calculate the standard deviation of the eight number counts. This same calculation is performed for various center coordinates distributed around the initial guess center with the same defined radius. The grid of the centers consists of every five pixels near the center in all directions and every ten pixels further away from it. This produces a map of coordinates with a standard deviation value associated to them. We fit a surface to this map using a two-dimensional spline smoothing technique developed by Wahba (1980) and Bates et al. (1986). The minimum point in the surface is our chosen center. The method can be used iteratively until the minimum lies in the finely spaced part of the grid.

All the simulated images have the center in the same position right in the middle of the chip. The size of the circle we use for our octants method is 170 pixels, which is slightly smaller than the radial extent of the simulated clusters. We calculate the distance between the measured and the real center (in x and y positions separately) for each of the five individual images in a given setup, then calculate the average and the standard deviation. Figure 1 shows the accuracy of the center measurements for all input power-law and King profiles. Results are shown for both the x and y coordinates in the case where we input 10,000 stars. We observe that the largest deviation is equivalent to 5 pixels for this group of simulations (0.5'' on the pixel scale of WFPC2). The center estimation improves with the degree of concentration of the cluster and with increasing number of stars. Similarly, the quality of the estimation decreases with decreasing number of stars and degree of concentration. As expected, this method works best when the SB distribution is not flat in the entire image.

2.3. Surface Brightness Profile

We test several different ways to obtain radial profiles on the simulated images. The profiles are obtained by measuring

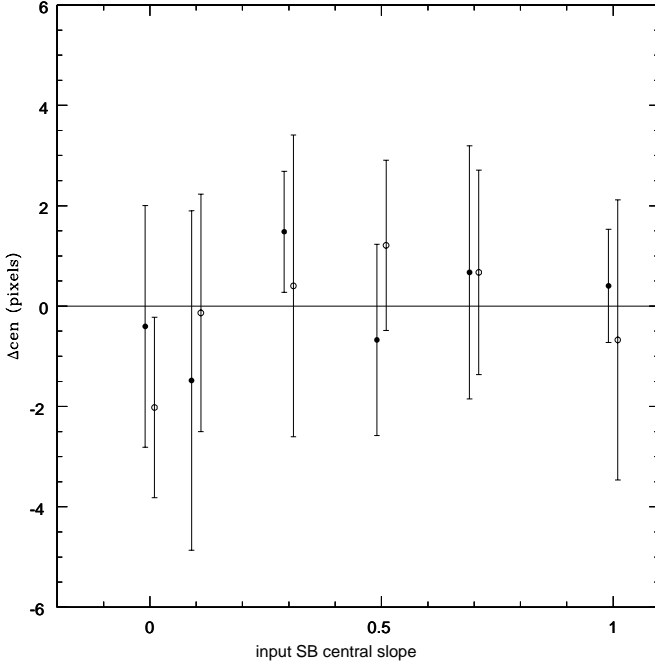


FIG. 1.— Comparison between the measured and input center for various sets of simulations with 10000 input stars. Zero slope is for the King profile case and the rest are for power laws. The average distance between the actual and measured center is shown for the x (solid points) and y (open points) coordinates in pixels. A small horizontal offset is introduced for clarity. Error bars are the standard deviation of the five individual measurements for each case. Each WFPC2 pixel is $0.1''$.

both integrated light and star counts. We note that both techniques have their advantages and disadvantages; for example, star counts can measure different radial profiles due to mass segregation while integrated light cannot. However, we argue that star counts are significantly less reliable compared to integrated light when trying to measure the global radial profile. When measuring integrated light, we use two different statistical estimators—the average and the biweight (Beers et al. 1990)—to get counts per pixel in a given annulus. Although the average is an optimally efficient estimator for central location when dealing with Gaussian distributions, it can be very biased when the underlying distribution is not Gaussian (i.e. having outliers). The biweight provides a robust estimate of the central location (i.e., mean) even when including a significant number of outliers. Since our images are made from discrete sources, there is a large number of ‘background’ pixels and a large number of ‘star’ pixels in each annulus, so the distribution is certainly not Gaussian. It is important to explore the effect of using a robust estimator versus using the average.

To measure star counts, we have to first measure the locations and brightness of all stars using DAOPHOT. We perform PSF fitting star subtraction on the images using the ALLSTAR routine with the same PSF we used to construct the image. This does not make the subtraction perfect since we introduced Poisson noise when constructing the images. Crowding and read noise have an important effect on DAOPHOT’s abilities to find stars. We observe this by comparing the number of input versus found stars in each simulated frame. For the 200,000 input stars case, ~ 3800 are found, while for the 50,000 input stars case, ~ 3000 . To avoid confusion in the following we refer to the groups of simulated images by num-

ber of input stars instead of number of detected stars. We now can measure integrated light in two different images, the original one with all the stars included (from now on called ‘full image’) and the one with stars subtracted, which is smoother (from now on called ‘subtracted image’). We use two sets of annuli to measure SB from integrated light; one has steps of three pixels from 1 to 20 pixels radius and the other has steps of twenty pixels between 10 and 200 pixels radius. The size of these annuli is a compromise between measuring at the smallest possible resolution and providing a smooth curve. The radius associated to each annulus is the midpoint between the outer and inner radii, while the surface brightness value is the number of counts per pixel divided by the number of pixels in a given annulus. We find that when using the average estimator, the profile obtained for integrated light is slightly biased and is very noisy, while the biweight estimator yields much smoother profiles with very little bias. The measurements on the subtracted image always yields a smoother profile than that obtained from the full one. Figures 2 and 3 show the input profiles together with the five individual measured profiles for various simulations with 50,000 input stars. We show a King profile, and the 0.5 and 1.0 power laws. In the cases of concentrated profiles and large number of input stars, both estimators produce shallower profiles toward the center for the subtracted images. The reason for this bias appears to be an over-subtraction near the center of the cluster stars where the crowding problems are worse. The program subtracts part of the background starlight as part of the stars which in turn produces a flatter looking profile near the center of the cluster. We also observe that the profiles obtained from the full image tend to look steeper than the input profile for the steepest power laws (inner slopes in the range $0.5 - 1.0$) as it can be seen in the leftmost panel of Figures 2 and 3. This is likely due to the contribution of the brightest stars near the center where integrated light is being divided into very few pixels, so the proportional contribution from the presence of a bright star is much larger near the center than in the outskirts. This effect can potentially be even larger for real clusters since they are known to have a degree of mass segregation (Howell et al. 2000), and therefore they have a larger relative number of bright stars near the center.

Since our goal is to obtain an unbiased smooth profile, we attempt alternative ways to measure integrated light profiles. One is to subtract only a percentage of the found stars, just enough to remove noise, but not so many that we get over-subtraction problems. We test for different percentages and compare them with a histogram of found stars in order to assess which stars are contributing to the observed bias. After extensive testing, we conclude that subtracting $\sim 10\%$ of the brightest stars is optimal. This normally subtracts the giant and horizontal branch stars leaving most of the main sequence. Another approach consists of masking a smaller percentage of bright stars. We choose a masking radius of 5 pixels; this takes care of a large portion of the light in each star, but it is small enough to avoid having too few pixels to sample in the central regions. In this case we obtain profiles with some amount of noise, but we eliminate the over subtraction problem. By eye inspection of the profiles (Figs. 2 and 3), it appears that the subtracted or the partially subtracted profiles are the least biased and/or least noisy way to recover the input profile for the shallower power-laws, while the masked profile is optimal to recover the higher power-laws.

We test the effect of changing the faint end of the luminosity function for the steepest power-law case by decreasing the

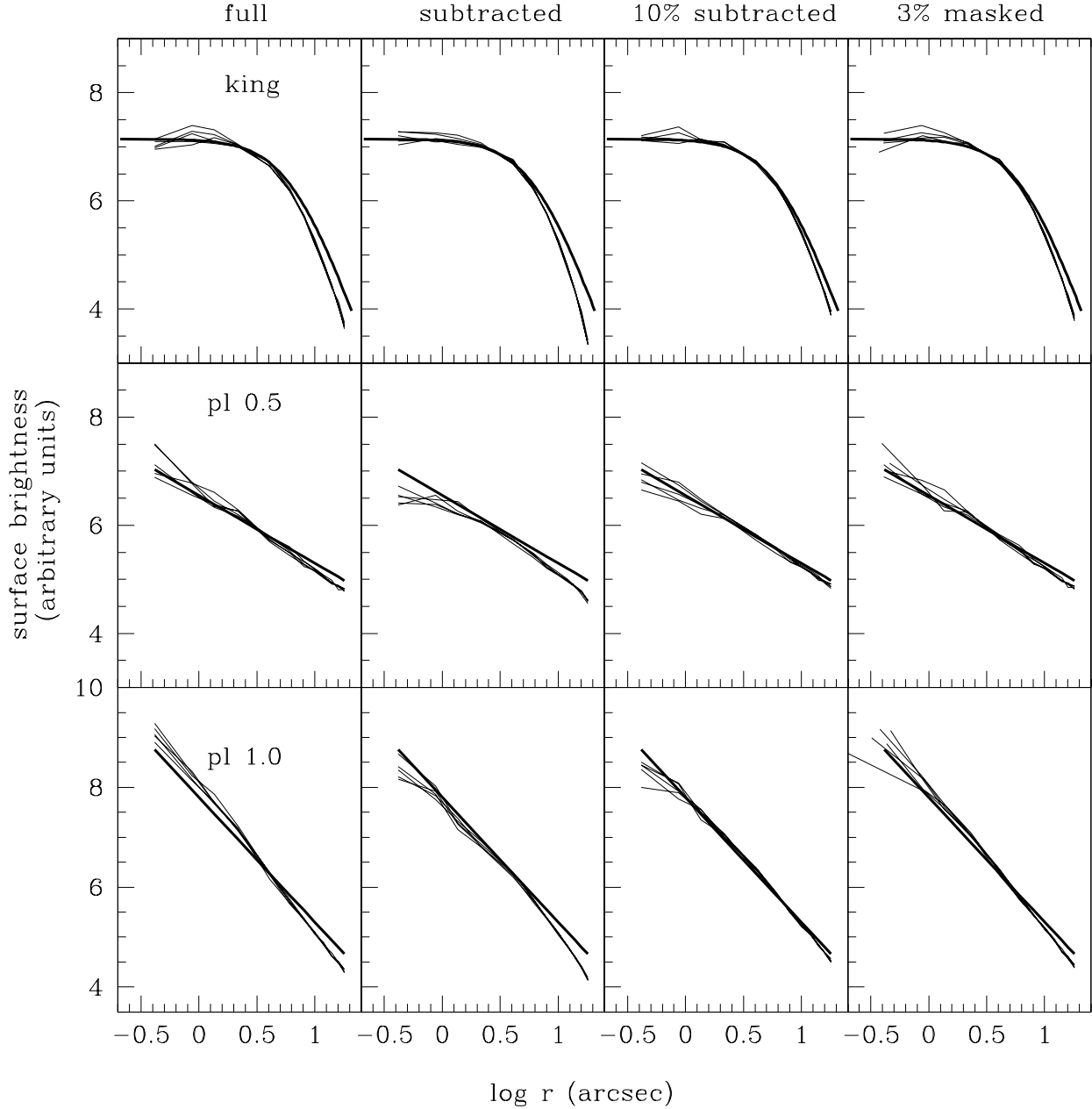


FIG. 2.— Surface brightness profiles for three groups of simulations with 50,000 input stars. For each case (King profile, 0.5 power-law, and 1.0 power-law) five individual measurements (thin lines) are plotted against the input profile (thick solid line). The profiles are measured from four different images: full, subtracted, 10% brightest stars subtracted and 3% brightest stars masked. The vertical axis is on an arbitrary magnitude scale.

number of faint stars. Our goal is to explore the effect of a change in background light on the central part of the profile. We normally use a luminosity function that rises all the way to stars 6 magnitudes fainter than turnoff stars (~ 18 mag). We change this to a flat distribution for the faint end (21–24 magnitudes), therefore having a lower contribution from background light. We find that the effect is negligible on the final profile; the central shape of the measured SB profiles was not affected by this change. Therefore, we conclude that the background light from very faint stars is not an important contributor to the central SB profile when measuring integrated light. This result implies that the possible effects of mass segregation are reduced when we measure the profile from integrated light, since the contribution to the profile comes from

stars with very similar masses. Therefore, the variations in the radial profile between the masses of those stars contributing to the integrated light are minimal. We also test for the effect of distance by using the same input lists for all cases, but making the stars two magnitudes brighter in one case and two magnitudes fainter in another. We obtain smoother profiles for the brighter case and a noticeable bias at large radii, where the profile is slightly underestimated. For the fainter case the profiles are noisier, but the bias at large radius seems to disappear (Fig 3). The over-subtraction related to crowding is amplified for the brighter case and smaller for the fainter case. M5 (the source of our luminosity function) has one of the brightest apparent magnitude horizontal branches in the galactic globular cluster system, so most of the actual observations will be

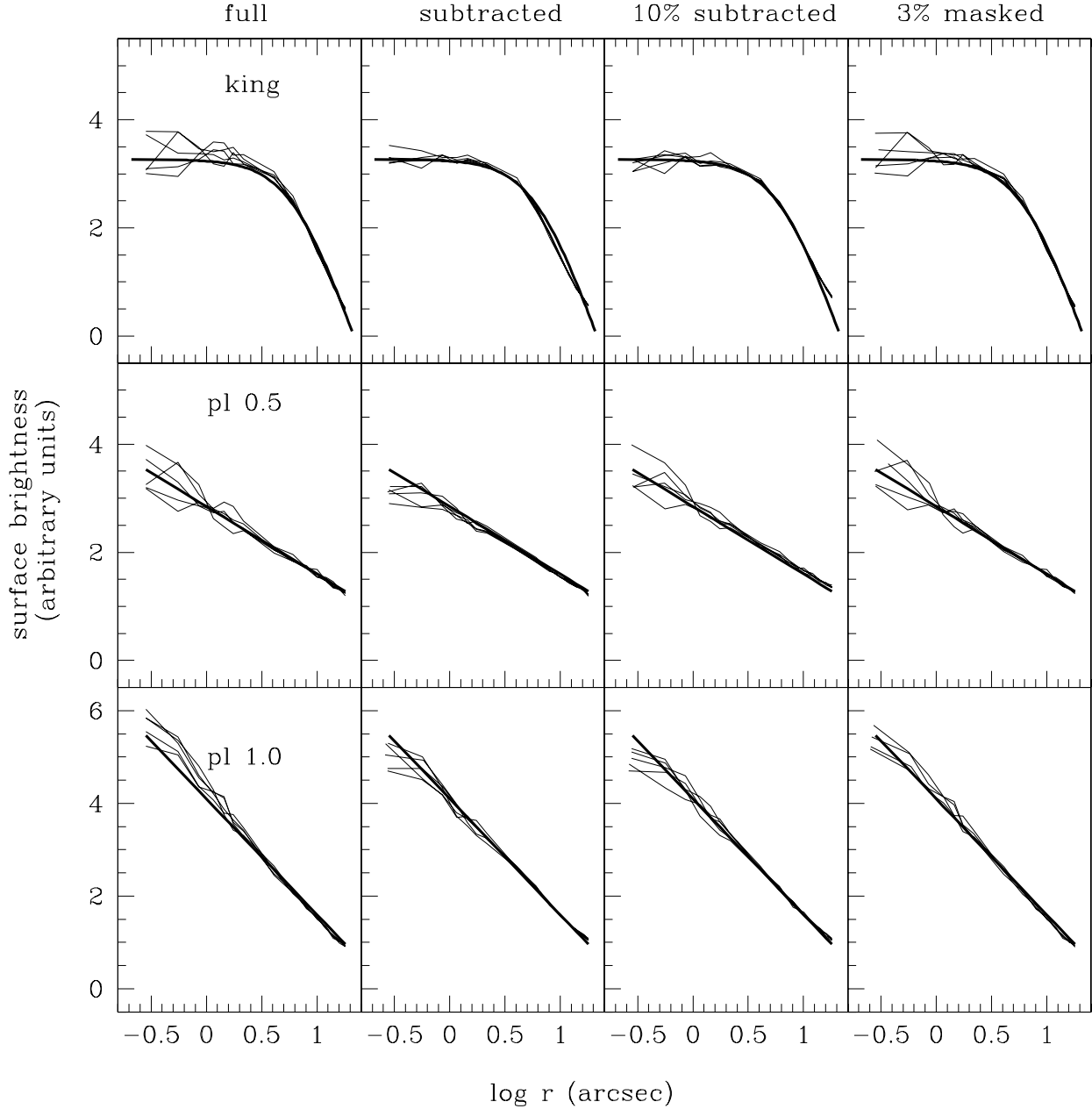


FIG. 3.— Same as previous figure but for simulations of fainter clusters. The groups of simulations were constructed by decreasing the brightness of stars by two magnitudes.

better represented by the simulated images created with the original and fainter star lists.

Star counts profiles are obtained in the same sets of annuli we use for integrated light. Due to crowding near the center of the images, only a fraction of the faintest stars are detected there. If we include those stars in the star counts, they tend to flatten the overall profile, particularly for the steep profiles and large number of input stars. As a consequence, we decide to use only the 50% brightest stars to construct this profile, since this is the limit where the shape of the input profile is recovered. In general, the star counts profile, as we construct it, can be used only as a comparison tool since it is too noisy to provide a robust result. It is worth clarifying that we do not apply any correction to star counts due to crowding, which is the normal procedure used by other authors to

obtain star counts profiles in these type of fields. At large radii, star counts are probably the only way to obtain a surface density profile. They are certainly the only way to measure the variation in profiles between different stellar groups within a cluster, which is something that cannot be measured with integrated light. However, at small radii, crowding effects severely limit the usefulness of star counts since they require a significant correction.

Surface brightness profiles obtained from integrated light can be noisy for some cases (least concentrated objects, lower signal-to-noise). Therefore, in order to measure inner slopes, we have to apply some kind of smoothing and check whether that smoothing biases our measurements. The smoothing technique is the one-dimensional version of spline smoothing mentioned in Section 2.2. It is based on the

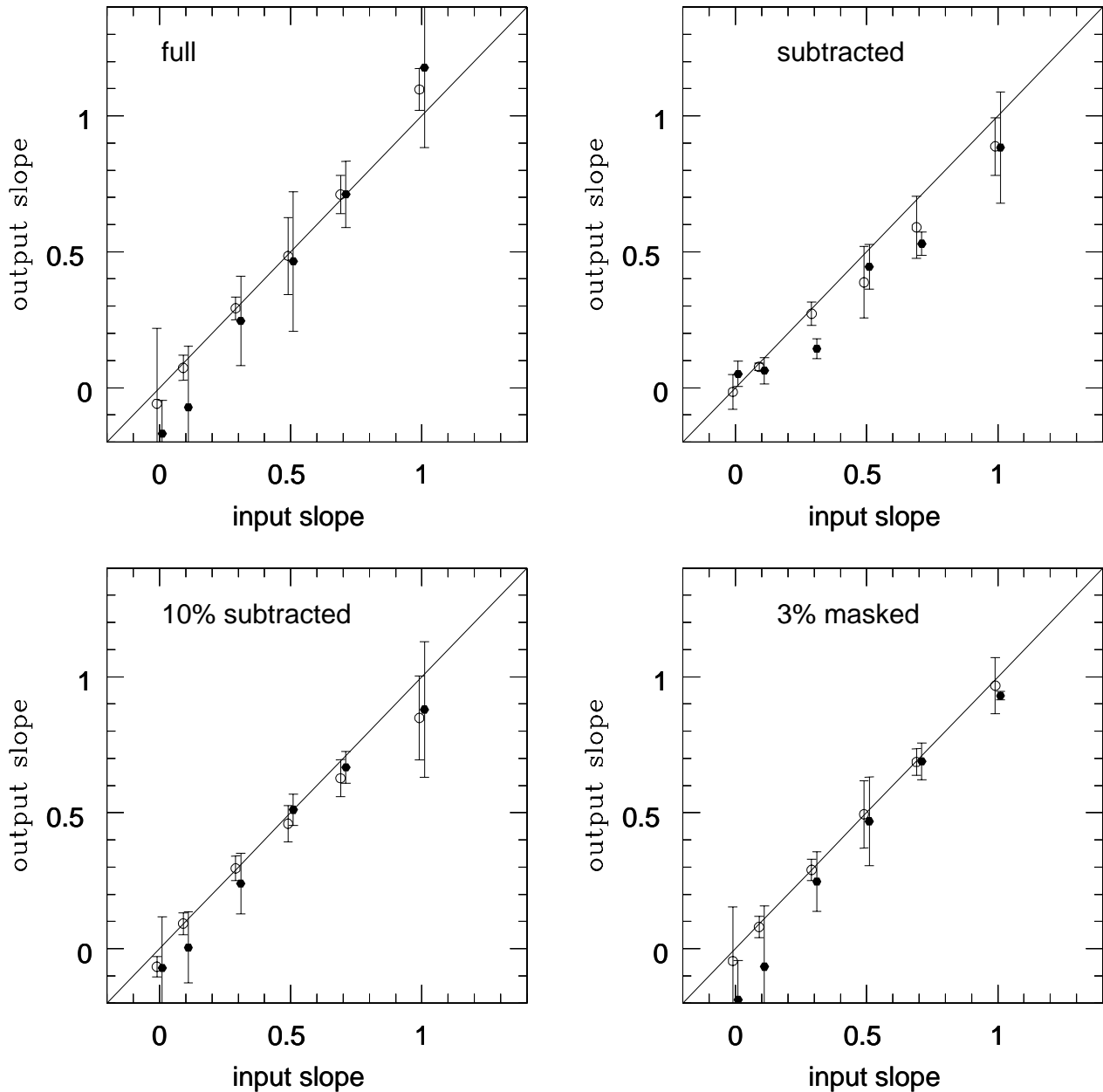


FIG. 4.— Input versus measured surface brightness slope for two groups of simulations. The open points show results for 10,000 input stars, the solid points show those for 50,000 input stars. A small horizontal offset is introduced for clarity. We show the average measured slope of the five individual profiles for each case. Error bars represent one standard deviation for the five measurements.

work by Wahba & Wang (1990) and described in detail in Gebhardt et al. (1996). We choose to apply a fixed amount of smoothing to every profile obtained in order to be consistent. The central slope is calculated by taking the derivative of the smooth profile on the few innermost points, which is equivalent to measuring at a radius of 3 pixels ($0.3''$ with the WFPC2 scale). Results are shown in Figure 4 for the 50,000 and the 10,000 input star cases. We plot input versus the average slope measured for the five realizations. The error bars represent the standard deviation of these measurements. Results confirm what the eye inspection of the profiles suggest. The subtracted and partially subtracted images yield a more reliable inner slope measurement than the full and masked im-

age for the shallow slope cases ($\beta < 0.3$), which seem to have larger error bars, particularly for the 50,000 input stars case. We confirm that using the masked profile for those with steep slopes is more reliable; subtracted and partially subtracted cases tend to underestimate the slope. In order to further estimate the scatter, we created twenty images using 50,000 input stars and 0.7 power law. These twenty cases do not include the five cases already analyzed. The standard deviation of the slope is slightly smaller for the twenty cases as for the five images, so the error bars calculated for the five simulations case are an upper limit.

Besides measuring the core radius (radius where the luminosity drops by half the central value) we are interested in

measuring the turnover radius (radius of maximum curvature) of the profiles. We do this by finding the minimum of the second derivative for the smooth profile. We created groups of simulations with small flat cores to test if we could detect such turnovers. Our results show that we can detect cores as small as $1''$ with our spatial sampling.

Given these results, we use the same four images (full, subtracted, partially subtracted, and masked) for the real data. If the four profiles obtained from these images are consistent we take the smoothest version (in general, this is the masked case). If they differ near the center (as it is expected for concentrated cases) then we take the profile produced from the masked image since that is the one that traces the cusps best. As a general rule we do not use the profiles obtained from the full image and from star counts because they appear to be biased for some cases and generally noisier than the rest.

2.4. Uncertainties in the Simulations

The uncertainties in the surface brightness are due to two sources when using integrated light: the photon noise and the shot noise from having a limited number of stars (i.e., surface brightness fluctuations). Thus, in order to get the real uncertainties, we have to estimate the shot noise from stars. Star counts, on the other hand, directly recover the appropriate noise, but at the expense of higher uncertainties due to the difficulties in measuring the individual stars (i.e., completeness due to crowding).

For the simulations, we have the knowledge of the actual shot noise since we know the input number of stars. In order to determine how to include shot noise, we run simulations with the same input parameters but a different star list. The scatter from these different realizations then provides the actual uncertainties including both photon noise and shot noise from the stars. However, with real data we do not have the luxury of running different star lists; therefore we have to find a way to determine the shot noise directly. We use a biweight estimate of the scatter and then apply a correction factor. The biweight scatter is determined from the scatter in the photon counts in the pixels for a given annulus. We then compare the biweight scatter with the scatter of the photometric points between the five different realizations. The ratio of the real scatter to the biweight scatter is larger for the simulations with smaller numbers of stars. Thus, we have to correct the biweight scatter by the appropriate amount. When using the data, we do not necessarily know the underlying stellar surface density, making it difficult to determine the appropriate scaling for the biweight scatter. However, we use an alternative method that relies on assuming a smooth radial profile. We discuss this method for real data in Section 3.5. Both methods give the same range in scalings, implying we have an robust estimate of the true uncertainties.

Alternatively, we could run proper completeness corrections and determine the corrected star counts. The standard technique would be to apply this as a function of magnitude and radius in order to determine the underlying luminosity function. With that in hand, one can straightforwardly measure the additional uncertainty due to shot noise alone. However, this will create an additional source of uncertainty due to the estimate of the completeness corrections themselves (the correction factors depend on the underlying distribution of stars which is precisely what is being measured, thereby causing a possible degeneracy). Another source of uncertainty is that star counts will always miss the contribution from the unresolved stars, which is not an issue for integrated light mea-

surements. Therefore, we rely on the above approach, and the one outlined in Section 3.5, where we calibrate the uncertainty estimates for the actual data with the simulations presented here. Since the simulations demonstrate that we recover the central shape accurately, our adopted approach is reliable.

3. DATA ACQUISITION AND ANALYSIS

3.1. Sample

HST has imaged a large fraction of all globular clusters in our galaxy. Piotto et al. (2002) obtained color magnitude diagrams for 74 galactic GCs from WFPC2 images. In addition, Mackey & Gilmore (2003b,a) obtained surface brightness for clusters in the LMC (53 objects) and SMC (10 objects), which we analyze in a future paper. Based on our simulations only a subset of the Piotto snapshot observations will provide a reliable SB profile since a minimum number of counts are needed in the frame. Given the distribution of concentration, total magnitude, and apparent magnitude of the horizontal branch only a fraction of the imaged clusters are useful. The requirement is to have enough total counts in the frame. This can be achieved by the cluster being near (bright horizontal branch), containing a large number of stars, or being very concentrated (but not dominated by one star). In general, detecting stars six magnitudes fainter than the horizontal branch with a signal to noise of 20 is a minimum requirement for low concentration clusters. This criteria can be relaxed for highly concentrated clusters ($c > 2.0$) and those with a large number of stars ($M_V < -7.5$). Using these criteria we gather from the *HST* archive a sample of 38 GC imaged with WFPC2. It is ideal to perform the study with images in U-band (F336) since giant stars contribute the same amount of light as main sequence stars at this wavelength, thus minimizing shot noise. Unfortunately, there are few images available with enough signal in U-band. Our selection criteria is using images observed in either V (F555), R (F665), or I (F814) filters and to have an exposure time of at least 100 seconds, although most of the images have exposure times over 500 seconds (see Table 1). After testing for consistency between filters (details below), we realize we can also include images in the U filter with long enough exposure times (> 1000 sec). The field of WFPC2 is $2.6'$ in size, which is adequate to measure out to ~ 2.5 half-light radius of most clusters but not out to the tidal radius. The scale of the CCD is $0.1''/\text{pixel}$ for the WF chips and $0.046''/\text{pixel}$ for the PC chip.

We use the WFPC2 associations from the Canadian Astronomy Data Center website¹. These images are spatial associations of WFPC2 images from a given target, normally coming from a single program. The individual raw data is processed through the standard calibration pipeline, grouped in associations and combined. The available data is a multi-group image with the images for the three WF and the PC chips.

3.2. Image Processing

We analyze the WFPC2 images using the same method applied to simulated images described on the previous section. Once we have an individual image for each chip, we trim the edges due to increased noise there. We use the "FIND" task on DAOPHOT to obtain a list of stars, followed by the task "PHOT" to perform preliminary aperture photometry. We construct a PSF for each of the four chips. After extensive testing for methods to automatize this process, we conclude

¹ <http://cadwww.dao.nrc.ca/>

that the best way to obtain a reliable PSF subtraction is to choose PSF stars by hand. A single bad PSF star has an important effect on the quality of the subtracted image. Once we have the list of PSF stars, we use an iterative procedure where a preliminary PSF is constructed, neighbors to the PSF stars subtracted, and recalculate the PSF. We also test constructing a PSF with spatial variations but in the end this does not have an effect on the quality of the measured profiles, so we construct a constant PSF for all images. In the end we have an image for each chip with all the stars subtracted and only background light remaining. We also produce images with only 10% of the brightest stars subtracted, and 3% of the stars masked as described in Section 2.3. A geometrical transformation of the individual images produces a mosaic image. We end up with four mosaic images for each cluster; one with all stars included, all stars subtracted, 10% of the stars subtracted, and with 3% brightest stars masked.

3.3. Cluster Center Determination

To determine the cluster center, we first transform all found stars to a combined coordinate list. We use transformations identical to those applied when making the mosaiced frame. With this master list we calculate both the center and radial density profile from star counts. The center is obtained with the method described in Section 2.2. The first guess center is made by visual inspection of the image when possible, then iterated until we find the best center. For the least concentrated cases ($\sim 30\%$ of the clusters) we have to make our initial guess using Digital Sky Survey images with a larger field. The radius for our method is chosen so that all the stars counted would lie within the chip containing the center of the cluster and it is always larger than the core radius. For two of the clusters (NGC 6624 and M69), the center is too close to the edge of one of the chips, so we had to use stars on the adjacent chip to find the center. For another case (M13) the core is larger than the chip so we also had to use stars in the adjacent chips. Three of the clusters have too big and sparse cores for this method to work (NGC 5897, M10, NGC 6712). For these cases we used the center indicated in the Harris catalog (Harris 1996); these cases are marked in Table 1 with an asterisk. It is worth mentioning that the sky coordinates reported in our table come directly from the WCS information contained on the header of the images, so they should be used only in the context of that specific image. We have noticed that the sky coordinates of a specific star can change by as much as $1.8''$ in two images with different headers due to *HST* pointing uncertainties. The differences between our center coordinates and those contained in Harris' catalog are discussed in Section 4.1.

3.4. Surface Brightness Profiles

With the center from the stellar data, we obtain a surface brightness profile from the integrated light in each of the four images. We do this by measuring a biweight (see Section 2.3) of counts per pixel on a given annulus, and then dividing that over the total number of pixels on the annulus. We use a different set of annuli for each object. Our goal is to obtain the best possible spatial resolution, while keeping the noise as low as possible. For each case there is a trade off between these two quantities. We also bin in order to have a good sampling around the 'turnover radius'. In the end we define three sets of concentric annuli: 3-7 pixels steps at 1-20 radius, 6-15 pixels steps at 15-35 radius, and 30-60 pixels steps extending the radial coverage to 800.

When we calculate the star count profile, as the analysis in Section 2.3 suggest, we cut the PSF subtracted star list to keep only the 50% brightest stars when we construct the profile. Stars are counted in the same annuli as the integrated light measurements and divided by the number of pixels in each annulus. In the end we obtain five profiles for each cluster from the full, subtracted, partially subtracted, masked images, and star counts. For most clusters the SB profile obtained from the full image or from the star counts are noisier compared to the others, so we never use them as the final profile. For the cases with steep cusps, there is always a difference near the center between the masked, partially subtracted, and completely subtracted profile, as observed for the simulations. In this case we always choose the result from the masked image since simulations show this is the least biased. For the cases where the masked, subtracted and partially subtracted profile have the same shape, we take the masked profile if it has the same amount of noise as the rest; but for a few cases we take either the subtracted (M3, NGC 6287, M92, and NGC 6388) or the partially subtracted (47Tuc, M79, M5, M80, M62, M9, M69, and NGC 6712) because they are smoother. These are all cases where the central profile is nearly flat.

If a very bright or saturated star lies near the center of the cluster it can have an important effect on the final profile, either because the PSF subtraction is poor or because of the presence of diffraction spikes that are not included in the PSF. From tests where we mask bright stars near the center of a cluster, we determine that they only affect the shape of the final profile if they are within 1 arcsecond from the center. M70 is the only case where we had to mask a bright star located within this region. Since this is a saturated star, we also mask the diffraction spikes. This occurs at the cost of decreasing spatial resolution because we cannot use the inner 5 pixels for our measurements.

The profiles that we recover sometimes differ greatly from previous ground based data. In order to check that this is due to improved spatial resolution, we bin one of our high signal to noise WFPC2 images to the reported pixel scale ($0.4''$) of the data used in Trager's catalog (Djorgovski & King 1986); we then convolve this image to account for the typical seeing reported for the observations in Trager's catalog ($\sim 2''$). We compare the profile obtained from this binned-convolved image with that obtained from the *HST* image. Fig 5 shows that the effects of pixel scale and seeing can hide a shallow cusp that can be well measured with *HST* resolution. While this effect has been well demonstrated for galaxies (Lauer et al. 1995), it has not been appreciated for clusters. The profile obtained from binning and convolving the image lies on top of the Chebychev polynomial fit to Trager's photometric points, while the *HST* profile is brighter near the center.

Another important test is to check for a possible filter dependence of the shape of the SB profile. M80 has observations available on F665 (780 sec), F555 (96 sec) and F336 (11,000 sec) filters. Figure 6 shows the SB profiles for each. We observe that the three profiles are consistent throughout the radial range, and they differ by the same amount from Trager's Chebychev fit. Thus, we use results from various filters. Obviously, color properties will cause some variations. Guhathakurta et al. (1998) report a $\Delta B-V \sim 0.3$ mag from $1''$ to $10''$ for M30. Since our main objective is to obtain the central slopes, the small color gradients will have little effect.

We also require surface brightness profiles extending out to large radii. The WFPC2 camera only covers the central region, and we must rely on ground-based observations. For

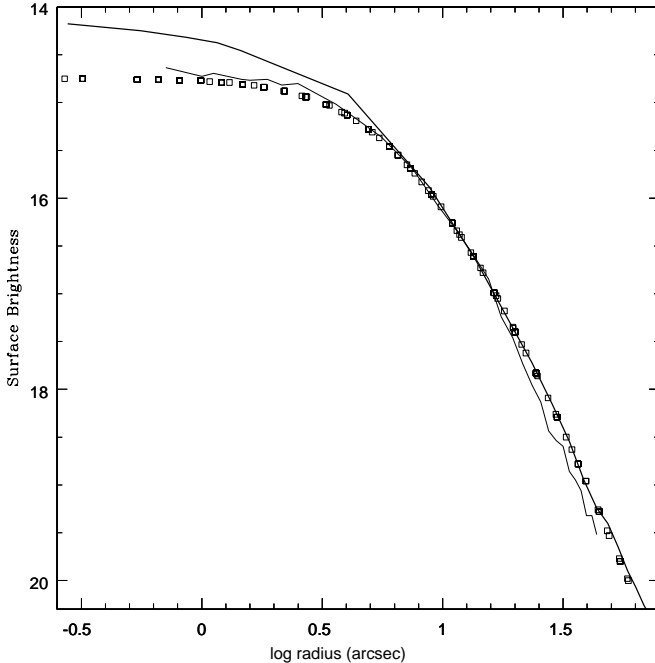


FIG. 5.— Surface brightness profiles for M54. The vertical axis shows a magnitude scale. The squares show the Chebychev polynomial fit from Trager’s catalog. The thick line shows the profile obtained from a WFPC2 image with our method. The thin line shows the profile obtained from the same WFPC2 when it is binned and convolved to mimic a ground based image. The change in the central SB profile is due primarily to improved spatial resolution from *HST*.

this, we use the Chebychev polynomial fit to the photometric points from Trager et al. (1995). We use our photometric points for the inner $\sim 20''$ and the Chebychev fit for the outer region. In a few cases the agreement between the polynomial fits and our results is good throughout, but for many cases there are discrepancies. We normalize the *HST* surface brightness to the ground based data by matching the two enclosed light profiles, calculated by integrating the SB profiles. As expected, the enclosed light curves differ in shape at small radius, but for most clusters, the curves have the same shape at large radius. Regardless of which filter is used to construct our profiles, the fact that they are all matched to photometric points in V and that the profiles are consistent between filters, brings all our photometric points to V magnitudes. There are a few clusters for which our normalization procedure is complicated (M70, NGC 6535, and M15). They all show a very steep profile through the entire radial range available in our images; since the ground based data show a core, the shape of the enclosed light profile obtained from *HST* doesn’t quite match that of the ground-based case. Uncertainty in this normalization does not affect the shape of the inner profile, but it will affect the value of central surface brightness.

After normalizing, the final surface brightness profile is a smooth version of the combination of our photometric points in the center and Trager’s Chebychev fits outside. The smoothing technique is the one described in section 2.3 for the simulated images. Once we have a reliable surface brightness profile, we deproject it to obtain the luminosity density profile. This is done by numerically calculating the first Abel integral, as in Gebhardt et al. (1996). The Abel integral uses the derivative of the SB profile so any amount of noise in the profile is greatly amplified. Therefore, we have to apply some

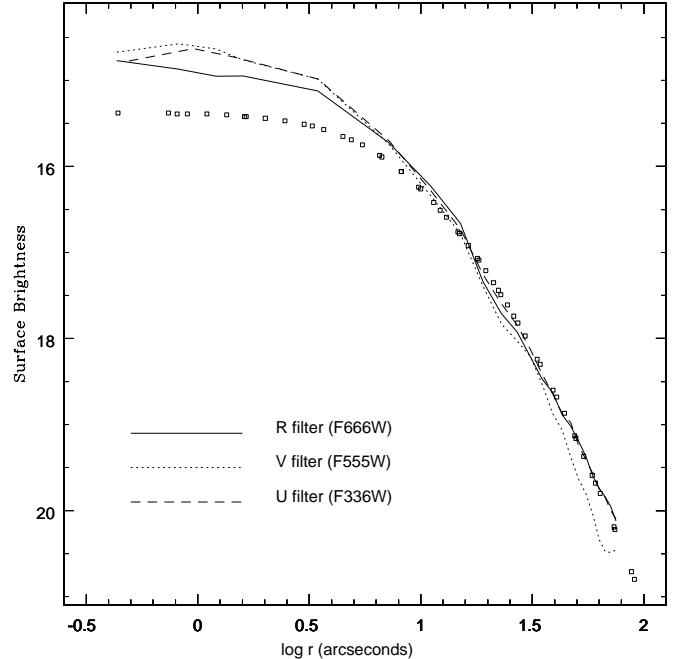


FIG. 6.— Surface brightness profiles for M80. The different lines show profiles in various filters (F336W, F555W and F666W). The vertical axis shows a magnitude scale. The squares show the Chebychev polynomial fit from Trager’s catalog (measured in V band).

amount of smoothing before deprojecting it (as described in section 2.3). Some clusters, particularly the ones with shallow cores, yield very noisy profiles near the center, making the process of deprojection challenging. For these cases we apply a pre-smoothing process where we substitute the innermost three or four photometric points by the average between their two adjacent points. In this way we can apply the same amount of smoothing to every profile in the sample. For a few cases, even if we apply the pre-smoothing procedure, we obtain a surface brightness profile that decreases slightly near the center, which produces a luminosity density profile with a negative density in the center and we cannot achieve a proper deprojection. For these cases, we set the central luminosity density slope to zero (marked with italics in Table 2).

We measure the central logarithmic slope of the smoothed surface brightness and luminosity density profiles by taking a first derivative with respect to the logarithmic radius. In the inner part of the profile, there is often a range where this derivative is constant, which implies that the profile has a constant slope in that region. We take the value of the derivative in this region as the inner slope for each cluster. The only exceptions are the objects which have steep cusps; for these cases, the slope changes through the entire radial range, so we take the value of the innermost points as the inner slope. Central slope measurements by other authors might be steeper for a given object, because they tend to fit a power-law in a more extended radial range (see example in section 4.3.3). For the cases where the SB logarithmic slope is slightly positive and we cannot achieve a deprojection, we just assign a zero value for the slope of the luminosity density. For these cases the values are written in italics on Table 2. We also measured the values of slopes in the region outside the core. In this case, since the values of the first derivative of the profile vary through this radial range we perform a least square fit to a line

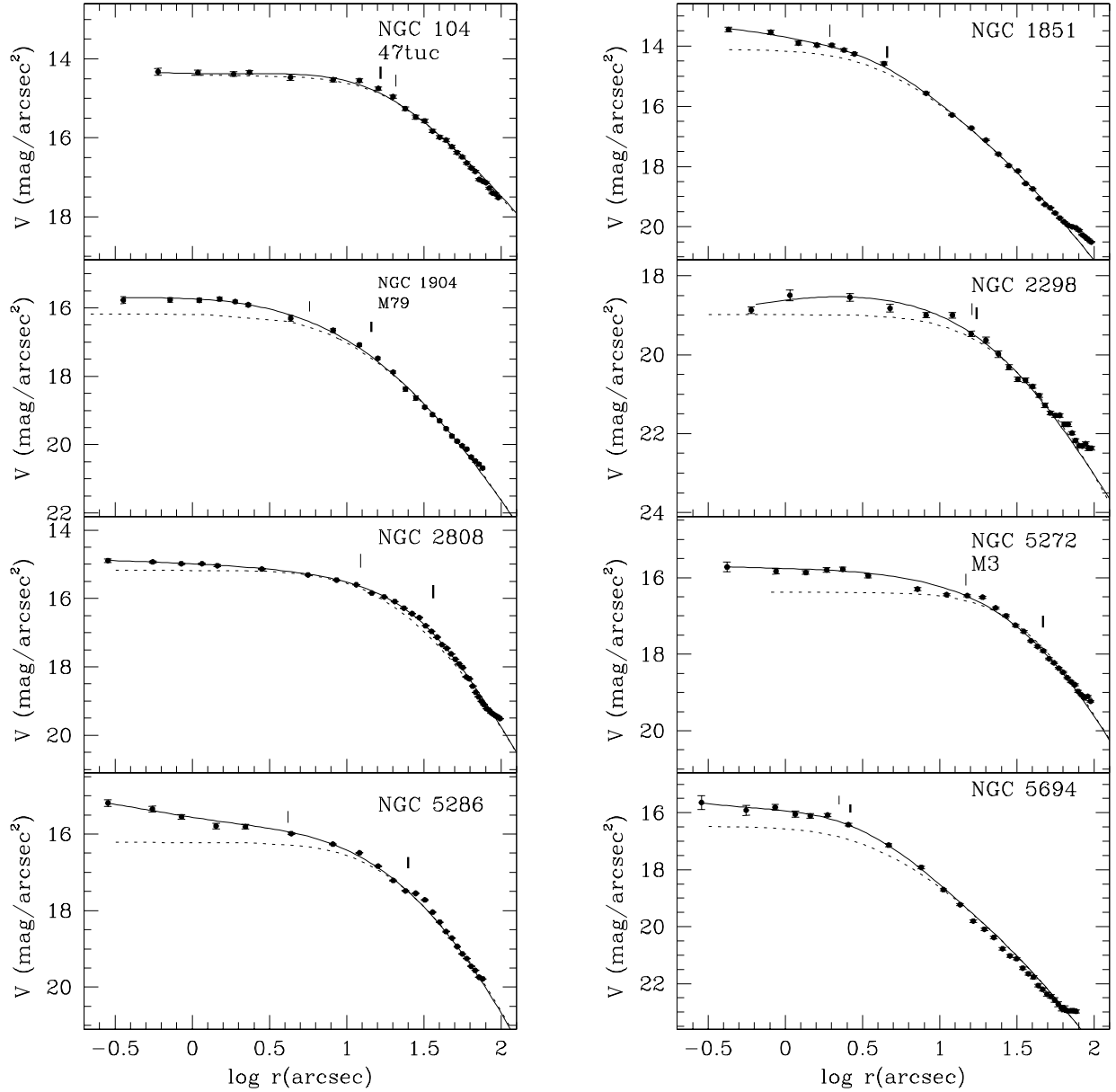


FIG. 7.— Surface brightness profiles for the entire sample. For each cluster we show our photometric measurements (solid points), our smooth profile (solid line), and Trager’s Chebychev polynomial fit (dotted line). The smooth profile comes from a fit to our photometric points inside $\sim 20''$ and the Chebychev fit outside that region. For every panel the SB units are $V \text{ mag/arcsec}^2$. We mark the location of the core (thin vertical line) and break (thick vertical line) radii. The core radius is where the central flux falls by half its value and the break radius is where the second derivative of surface brightness with respect to radius reaches a minimum.

for the smooth profile.

Since we are re-deriving SB profiles, we need to measure core radius as well. Historically, the core radius has been considered as the radius where the value of the flux falls by half the central value. The radius often coincides with the radius where the profiles seem to turn over and change slope, which we call break radius. We distinguish these two radii for our profiles. The core radius is calculated by taking the central surface brightness and finding the radius where the flux falls by half this value. We should note that the central surface brightness is measured as the value for our innermost data

point, therefore, this value of core radius is resolution dependent for the non-zero slope cases. We also calculate a break radius by finding the radius that corresponds to the minimum of the second derivative of the smooth profile. This is the radius where the slope of the profile changes by the largest amount, so it can be seen as the turning point for the curve. Both radii are presented in Table 2. For the cases with slopes less steep than -0.5 , where we can measure a break radius, we compute the ratio of the smallest resolution radius with break radius. For all cases this ratio is smaller than 0.15, which means that the break radius is at least 6 times larger than our

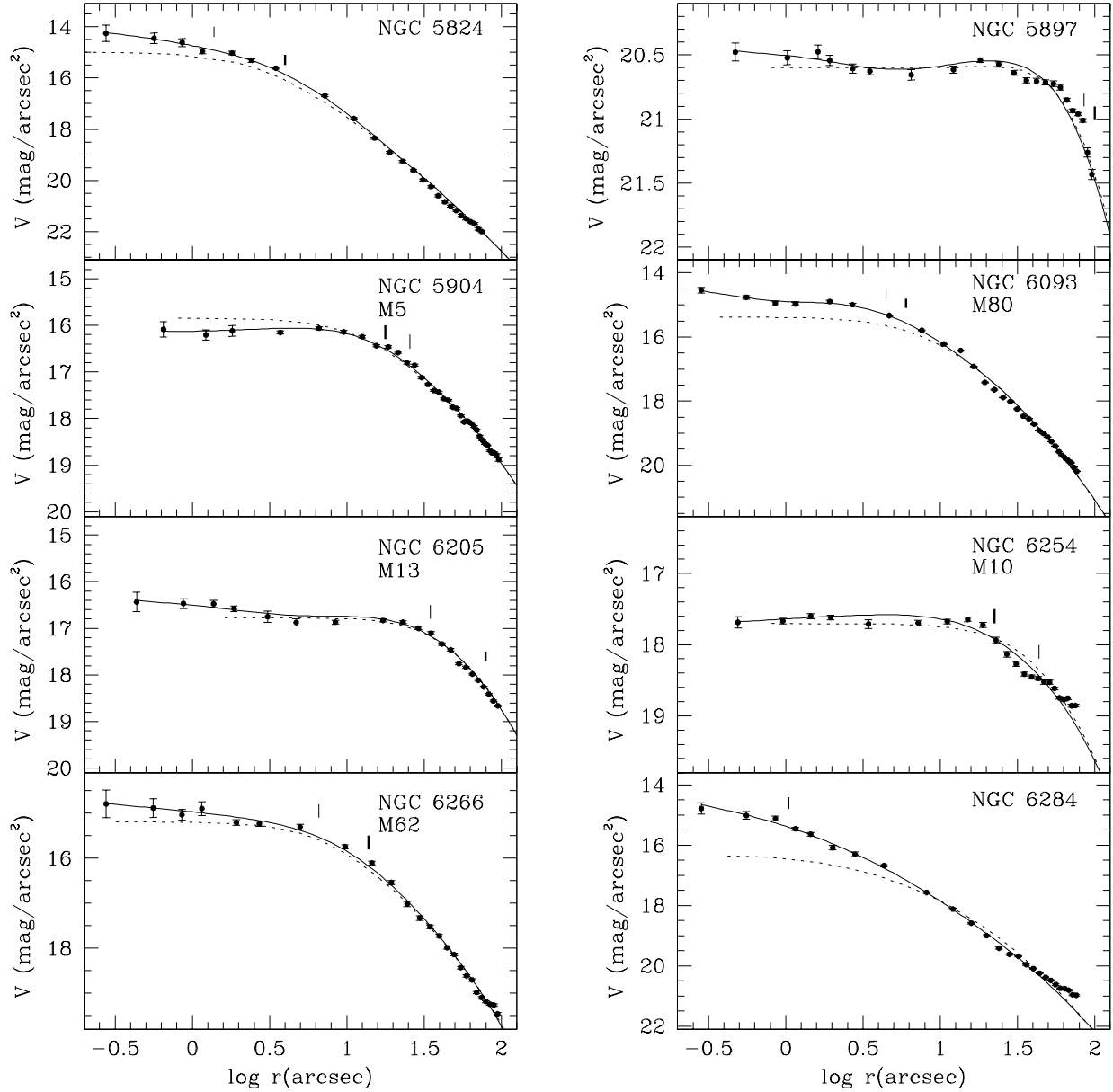


FIG. 7.— continued

smallest resolution radius. We plot this ratio versus the measured value of central SB slope and find no correlation. In this way we are confident that our reported values for central slopes in the weak cusps cases are well within the observed core of the clusters and the slope value is not due to lack of resolution.

3.5. Uncertainties for the Data

In Section 2.4, we describe how we estimate uncertainties for the simulations, which are based on different realizations where we can include the shot noise from stars directly. Here we describe the method we used to calculate the uncertainties for real data and we calibrate these method against that used for the simulations. We assume that the underlying stellar

radial profile is smooth. Then the uncertainties of the photometric points should reflect deviations from a smooth curve in a statistically meaningful way (i.e., have a Gaussian distribution around the mean value). From the photometric points, the biweight yields an estimate for the central location and scale (scatter); this scale value is divided by the square root of the number of sampled pixels and used as the initial uncertainty for individual photometric points. We then calculate the root mean square (RMS) difference between the smooth profile and the data points for the central region. The ratio of the biweight to the RMS should represent our lack of inclusion of shot noise from the stars. This ratio depends on the extent of the radial bins (i.e., the number of pixels used), therefore we use two different scalings for the different bin-

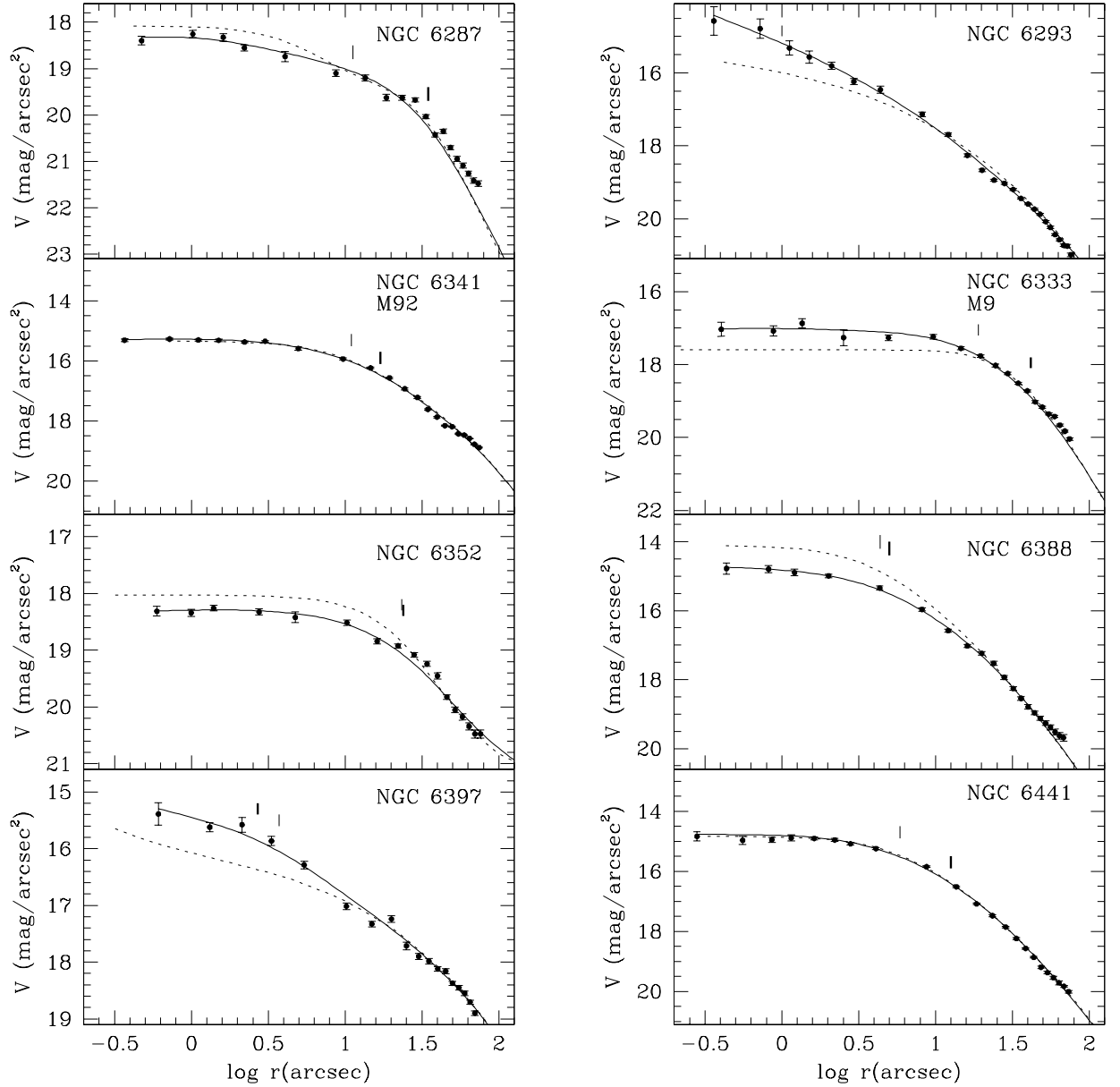


FIG. 7.— continued

ning. The average scaling for the inner points is about 2 and about 7 for the outer points. These numbers are consistent with what we found in the simulations. Thus, we are effectively including shot noise from stars. The largest scalings occur for sparse clusters (NGC 6397, NGC 6535 and NGC 6752), as expected.

We calculate the uncertainties on slope measurements from a bootstrap technique and compare these with the values measured for simulated images. The bootstrap approach follows that in Gebhardt et al. (1996). From the initial smooth profile, we generate a new profile by generating random values from a Gaussian distribution with the mean given by the initial profile and the standard deviation from the photometric uncertainties. We generate a hundred profiles in this way and

measure the 16-84% quartiles for the errors. Independently, each cluster is associated to one of the simulated cases according to its concentration and number of detected stars, and the standard deviation from Fig 4 is taken as the uncertainty. These two independent error measurements agree quite well, which gives us the confidence that the uncertainties calculated with the bootstrap method are reliable. Table 2 presents this results. The uncertainties for luminosity density slope measurements is also obtained from the bootstrap calculation. We do not estimate uncertainties in luminosity density slope for those cases where we cannot achieve a deprojection. We performed one more sanity check on our slope uncertainties by measuring the effect of increasing the uncertainties on photometric points by a factor of two. From the bootstrap method,

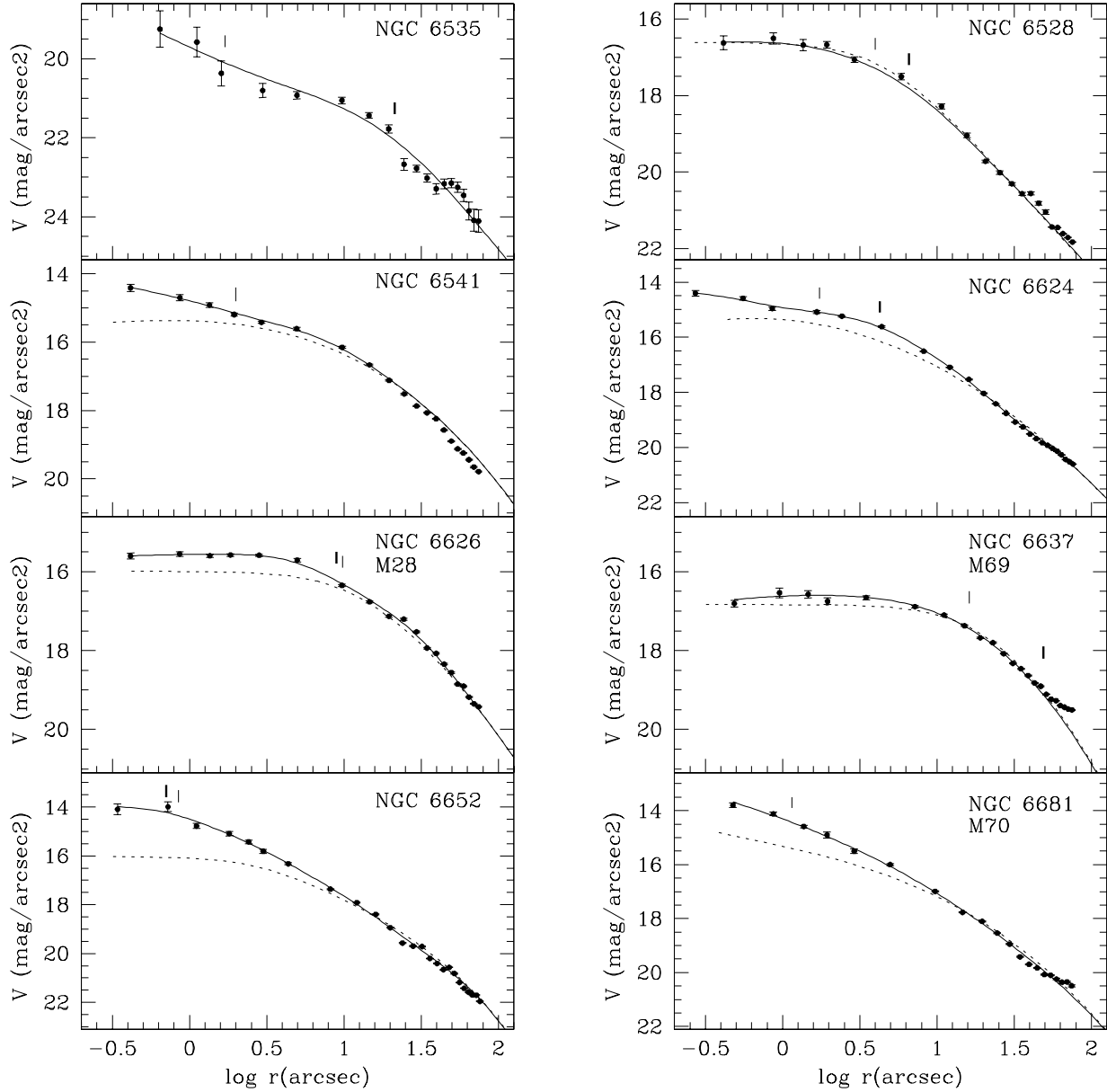


FIG. 7.— continued

we find that the slope uncertainties increased by a modest factor, less than two, for most clusters. Thus, the slope uncertainties are not too sensitive to individual photometric errors.

4. RESULTS AND DISCUSSION

4.1. Surface Brightness and Luminosity Density Profiles

We compare our measured centers (Table 1) with those listed in Harris' catalog (Harris 1996). For 66% of the sample the difference is less than five arcseconds, 24% of the objects have a difference between 5'' and 10'' and only 10% have a difference larger than 10'' (NGC 1851, M3, NGC 6541 and M2). As mentioned before in Section 3.2, for three of the clusters (NGC 5897, M10 and NGC 6712) we used the center listed in the catalog as our center. For the most concentrated clusters,

even a one arcsecond miscalculation of the center can flatten the central part of the profiles; so this might be another cause for missing weak cusps in previous measurements.

The SB profiles for the whole sample are shown in Figure 7. For each cluster we show the SB values measured from the image, the smooth profile, and the Chebychev polynomial fit obtained by Trager et al. for comparison. We warn the reader that, as explained in detail on section 3.2, the photometric points beyond $\sim 20''$ do not participate in the fitting of the smooth curve, instead, the Chebychev fit is used in this region. For most objects the agreement between the ground based data and ours is very good at large radii ($> 10''$). There are a few cases that show disagreement between the two profiles; these clusters tend to show a steep inner profile

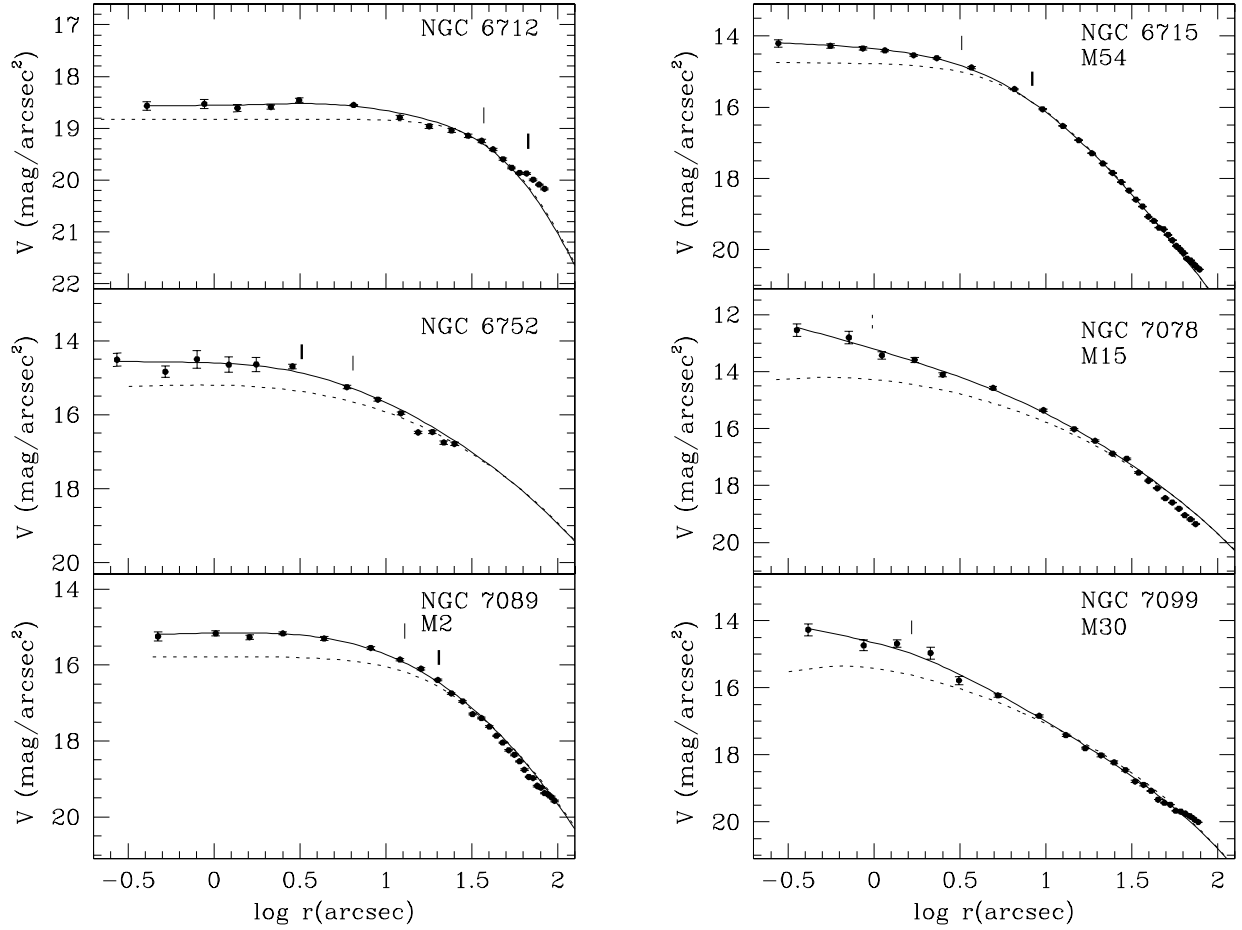


FIG. 7.— continued

(NGC 6284, NGC 6535, M70, M15), with the largest discrepancies in the inner 10 arcseconds. As we already discussed (Section 3.2) these differences may be due to PSF effects. We observe that for 70% of the sample the central photometric points are brighter than the polynomial fit obtained from ground based photometry, sometimes changing the shape of the previously measured central surface brightness (i.e., making it steeper). The remaining 30% agree with previous measurements or have fainter photometric points near the center. For the extreme cases, the difference between the central SB value with previous reports is larger than 1.7 magnitudes (NGC 6284, NGC 6535, NGC 6652 and M15).

In order to check for any potential biases from our smoothing in the central regions, we compare with single-mass King profiles (King 1966) fitted to the combination of our photometric points and Trager’s Chebychev fit. For these fits we keep the value of the tidal radius fixed (from Trager’s values) since our data is only in the central regions. Figure 8 shows representative fits for three clusters, 47Tuc, NGC 2808, and NGC 6293. For 50% of the sample, our smooth profile and the King fit are equally good fits to the data, as in the case of 47Tuc. For the other 50%, we obtain either a small departure from a flat core, as in the case of NGC 2808, or a clear large departure as in the case of NGC 6293. These departures

are always in the same sense, i.e., the photometric points are brighter than the King fit towards the center and the deviation increases as radius decreases. We also performed power-law plus core fits with the functional form used by Lugger et al. (1995). We only performed these fits for the cases that depart from a King profile. The fits are performed using only the datapoints for the central arcminute, since we do not expect the outer part of the profiles to be described by a power-law. For most cases, the power-law plus core fit follows the same trend as the King fits, but for NGC 6397 and NGC 6652 these fits are as good as our non-parametric profile. We discuss the details for each object in Section 4.3.

All of the clusters previously reported as core-collapse show cusps, with the exception of NGC 6752, which shows a flat core. Only four of them (NGC 6652, M70, M15, and M30) show a ~ -1.6 central logarithmic slope in luminosity density, which is normally assumed for objects in this state (Breedeen et al. 1994). The rest have slopes between -1.2 and -1.4 . We consider all objects with luminosity density slopes more negative than -1.0 to have ‘steep cusps’; they constitute 34% of the sample. 24% show weaker cusps with luminosity density slopes between -0.2 and -1.0 ; many of these have been previously reported as flat cores or were marked as possibly core collapse on Trager’s catalog. We consider

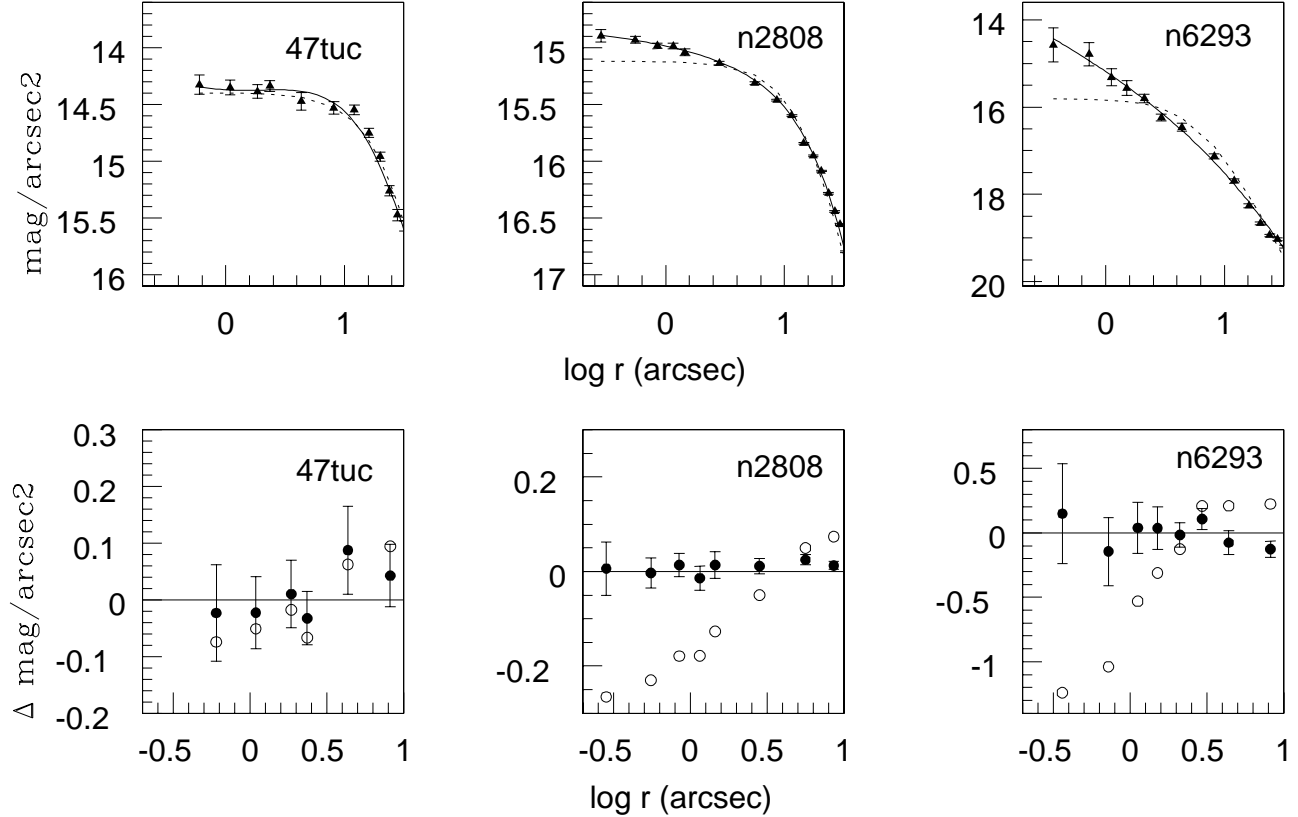


FIG. 8.— Representative single-mass King fits for 47Tuc, NGC 2808, and NGC 6293. The top panel shows the photometric points (triangles) along with our smooth fit (solid line) and a King fit (dotted line). The bottom panel shows the residuals for the smooth fit (solid points) and for the King fit (open points).

these objects to have ‘weak cusps’. Finally 42% of the objects in the sample show flat cores consistent with an isothermal distribution, even when their inner photometric points are brighter than previous measurements. If we group the weak cusps with the steep cusps, in total 58% of the sample do not show isothermal cores. The presence of so many non isothermal cores will have important consequences for the dynamical evolution of the clusters. No dynamical model or simulation predicts this distribution of slopes for GCs. Grillmair et al. (1995) make a detailed study of large radial structure for 12 galactic clusters. They obtain surface density profiles from star counts and find that most of the clusters depart from the King models previously fit to them because they contain stars in the extra tidal region. This result put together with the fact that more than half of the objects in our sample are not represented by isothermal cores leads us to think that King models do not describe well the surface density profile of many globular clusters.

Our measured errors for surface brightness slopes are on average 0.1 and the largest is 0.18. For the luminosity density slope the average is 0.28 and the largest error is 0.54. For the cases with steep cusps, the error is always under 0.35. Those with measured SB slopes under -0.2 are all $2\sigma+$ detections, implying that they show a deviation from an isothermal core. Assessing the uncertainties for the flat cases is particularly relevant since we want to evaluate the possibility of having positive slopes. Luminosity densities with a central minimum have been observed in a handful of galaxies (Lauer et al. 2002). These have been interpreted as two possible scenarios: one where a stellar torus is superposed on a normal core due

to a recent merger (this is quite unlikely in a globular cluster), and the other scenario where stars are depleted from the center due to a binary black hole interaction. Unfortunately, the uncertainty in our measurements for cores with positive slope is large enough to include zero slope.

For each profile on Fig 7, we mark both the core and the break radius. Seven of the steep cusp cases do not have a measured break radius because they do not show a clear turning point in the profile. We observe that for the rest of the sample these two radii do not always coincide. For all but six cases, the break radius is larger than the core radius, while for five cases the two are the same. The core radius that we report is a non-parametric fit as opposed to its historical value as one of the parameters for King fits.

We also check whether our limited spatial resolution (about $0.3''$) has an effect on being able to resolve a core. We plot the ratio of our smallest resolution over the measured break radius against various properties; this ratio is always smaller than 0.2 implying we have at least five resolution elements inside the break radius for those clusters that have a turn-over in the light profile. We find no correlations; if all clusters have King-type profiles with small core radii, we would expect to see correlations.

4.2. Slopes Distribution and Correlations

Figures 9 and 10 show histograms of the surface brightness and luminosity density logarithmic slopes. There is no clear separating line for two classes of objects, so the sample cannot be cleanly divided into isothermal and core collapse profiles. Since our sample is only $\sim 30\%$ of the full galactic globular

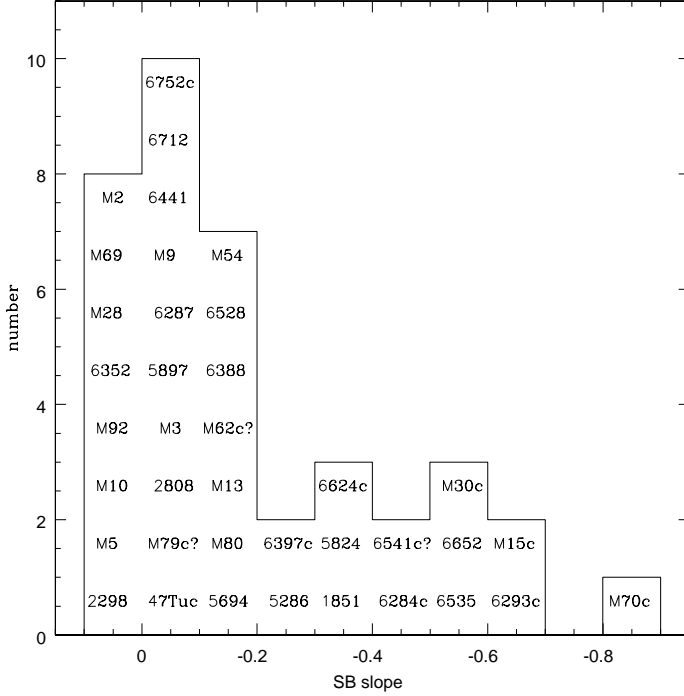


FIG. 9.— Histogram for surface brightness central logarithmic slopes. Individual clusters are shown in each bin. The name of the cluster is coded according to previously reported dynamical state in Trager’s catalog. Marked with a ‘c’ for core collapse, ‘c?’ for possible core collapse and just the name for flat cores.

cluster system, we have to determine potential biases. Trager et al. classify 16% of their sample as core collapse clusters and 6% as possible core collapse (‘c’ with a question mark in his catalog). Our subsample has 21% objects considered core collapse and 8% possible core collapse from Trager et al. Thus, our sample resembles the distribution for the full sample with a slightly larger number of core-collapse cases. All but one (NGC 6752) of the objects marked as core collapse fall in our ‘steep cusp’ category, while those clusters marked as possible core-collapse are found in all three categories. We find 17 objects previously classified as flat cores (i.e. classic King models) that are consistent with an isothermal profile. We can determine the fraction of clusters that have isothermal cores by comparing our SB histogram with that expected given our measurement uncertainties for the clusters that have nearly flat cores. Our average slope uncertainty is about 0.1. A Gaussian that contains 50% of the sample with mean 0 and sigma 0.06 (the average slope error for flat cores) matches the flat end of the slope distribution very well. The remaining population ($\sim 50\%$ of the objects in the sample) shows a fairly uniform number of objects between slopes -0.2 and -0.8 . Thus, only half the objects in our sample are consistent with a King-type profile.

We need to compare the slope distributions with theoretical models for globular clusters, particularly for those clusters with non-zero slopes. As discussed in Section 1.2 there have been two mechanisms explored for producing cusps in these systems: core-collapse and the presence of an intermediate mass black hole in the center of the cluster. The range of 3-dimensional density slopes is narrower for black hole than for core-collapse models, but they both center around the same number ~ -1.65 . However, only the clusters with the steepest profiles in our sample fall in this range. In the case of

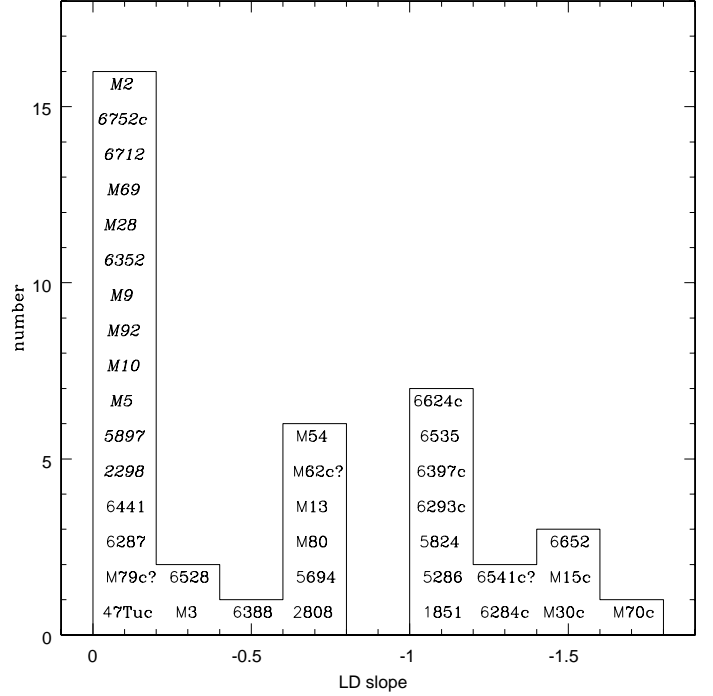


FIG. 10.— Histogram for luminosity density central logarithmic slopes. Cluster names are coded as in previous figure. Clusters in italics are those for which deprojection cannot be achieved due to diverging density profile near the center.

core-collapse the slope depends on the mass of the stars used to construct the profile, so this could extend the range toward shallower slopes. Another factor is the time dependence of the core-collapse model when they go through the gravothermal oscillations. According to Fokker-Planck simulations, a star cluster will spend a considerable amount of time in between successive collapses, where the light profile resembles a King model with a flat core. Unfortunately, these models do not give enough details about the slope of the density profile or the time spent on intermediate stages, so it is difficult to say if the slope of our ‘weak’ cusp clusters are consistent with this picture or if we need to invoke a new mechanism to explain this shallower but non-zero slopes. We note that Dull et al. (1997) model M15 as an intermediate stage of core-collapse. Since M15 has one of the steepest profiles in our sample, then it appears that even invoking this phase, it is unlikely to reproduce the full range that we find.

An alternative explanation for the existence of intermediate slopes is presented by Baumgardt et al. (2004). They perform detailed numerical simulations of clusters containing an intermediate-mass black hole in their center. Their results show that the surface brightness profile after a Hubble time shows a shallow cusp with slopes around -0.25 , and clearly distinguishable from zero. There are at least 8 objects in our sample that fall into this category, but without complementary kinematical measurements this hypothesis cannot be confirmed.

We plot logarithmic SB and LF central slopes against a variety of global properties of clusters taken from Harris’ catalog or measured in this work. Figures 11 and 12 show these plots for both central slope values versus central surface brightness, total V magnitude, metallicity, logarithmic physical core radius, logarithmic physical break radius, logarithmic half-

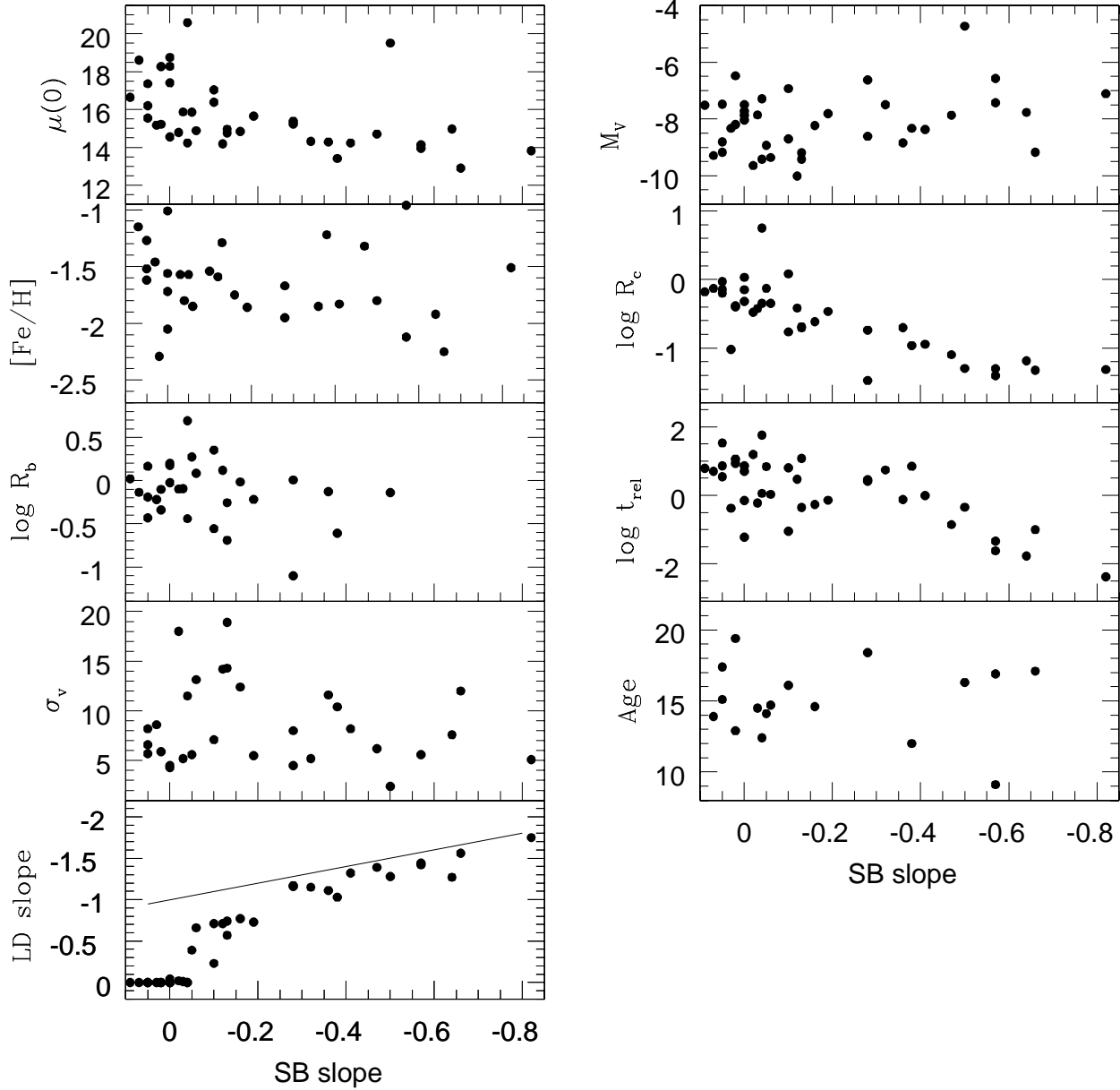


FIG. 11.— Surface brightness central logarithmic slope versus central surface brightness, absolute total V magnitude, metallicity, logarithmic core radius (in parsecs), logarithmic break radius (in parsecs), half light relaxation time, velocity dispersion, logarithmic age and luminosity density slope (the solid line represents ‘LD slope = SB slope + 1’). The distances to the clusters were obtained from Harris’ catalog. There is a trend between central surface brightness and slope (with one obvious outlier). There is also a trend with core radius and relaxation time.

light relaxation time, velocity dispersion and age. Fig 11 also shows the relation between SB slope and LF slope. We observe some global trends. As it is to be expected, the clusters with steep profiles tend to have brighter central surface brightness values, although the very sparse cluster NGC 6535 is an outlier. There is an indication that objects with steeper cusps are found in smaller objects (i.e. higher total magnitude); this trend is more clear for luminosity density slopes. Metallicity measurements do not appear to show any trend. The same is true for galactocentric distance, except that the objects with steeper cusps are all close to the center of the galaxy, but given the size of our sample this might just be a small number effect. Half-light relaxation time seems to be

shorter for the steep cases. As it is to be expected, the core radius is smaller for clusters with steep profiles, while the break radius shows no correlation with slopes. Velocity dispersion and age show no correlation with slopes. Finally, the relation between surface brightness and luminosity density slope is not linear, as expected, and is similar to that observed for galaxies (Gebhardt et al. 1996).

The measured values for outer slopes range from -1.0 to -2.5 for the clusters in the sample. When we plot these outer slopes values versus global properties, and in particular versus either central SB slope or concentration, we find no correlations. So as far as this sample goes, we cannot distinguish between King-type or core-collapse objects from the outer slope

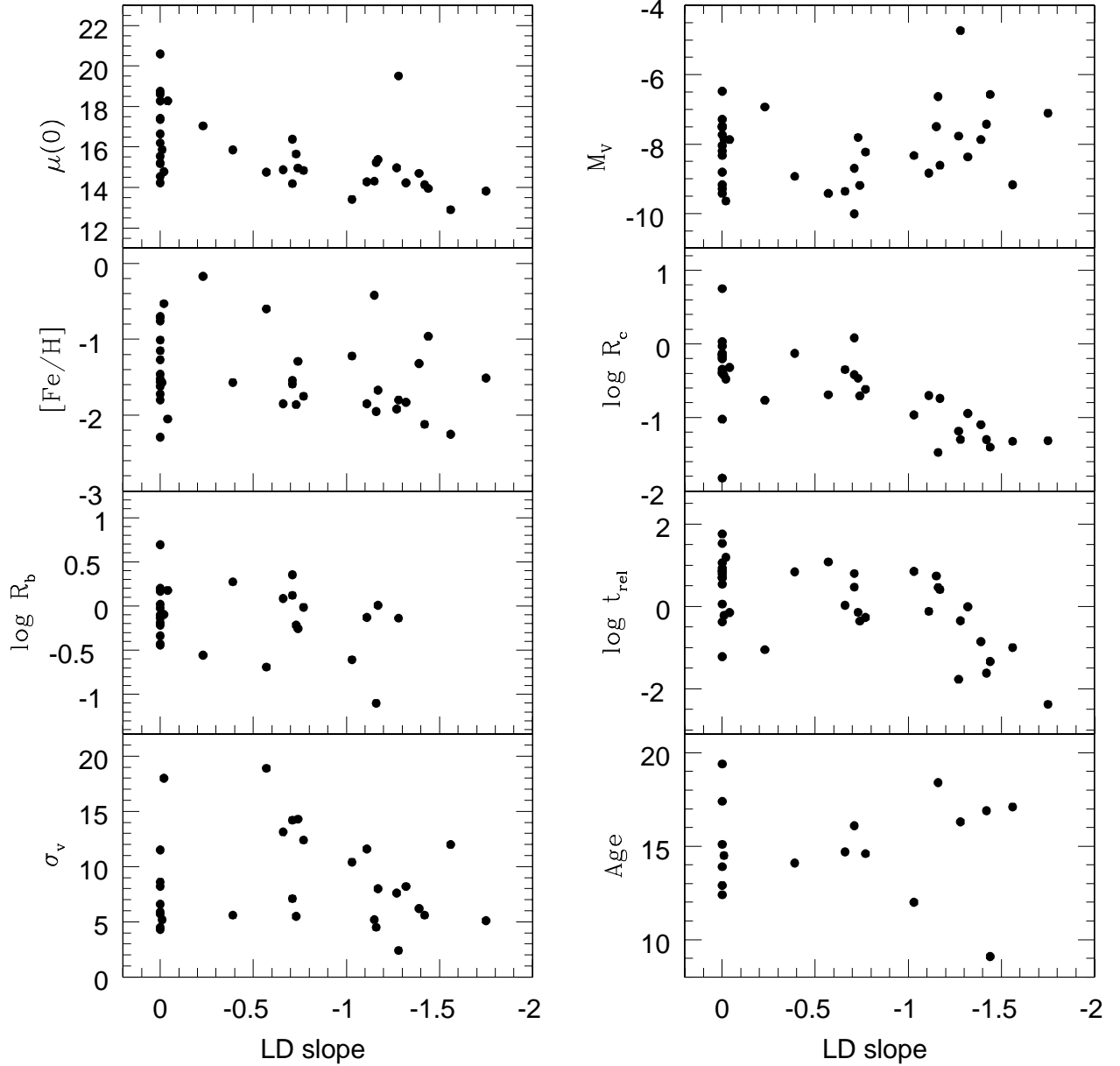


FIG. 12.— Luminosity density central slope versus central surface brightness, absolute total V magnitude, metallicity, logarithmic core radius, logarithmic break radius, half light relaxation time, velocity dispersion and logarithmic age.

of the profiles. This is illustrated on Fig 13 where we overplot all the observed profiles, scaled in surface brightness and either their break radii (when they exist) or core radii (for the others). The profiles are color coded according to the classification given above for flat cores, weak cusps and steep cusps. It can be observed that although the different groups can be separated in the inner region, they do not seem to split into groups in the outer region. This figure confirms once again that the profiles cannot be clearly divided into flat cores and steep cusps, but that they span a continuous range of central profiles.

4.3. Individual objects

4.3.1. NGC 6397

NGC 6397 is a peculiar object because it has always been considered to be in core collapse due to its steep inner profile, but unlike other objects considered to be in core-collapse, this one shows a sizable core. Lugger et al. (1995) report measuring a $4\text{--}10''$ core. Our measurement for the break radius for this cluster is $2.1''$. We fit a power-law plus core function for the central region of the profile and we find that the fit with a $4.5''$ core radius is a good fit, but only for the central $10''$. It could be the case of a partially resolved core. In previous studies the inner slope is measured in a radial range extending well beyond the measured core radius (as far as $100''$). We measure inner slopes at the central few arcseconds for all objects in our sample, therefore our slope value for this object is much shallower than previous measurements. Our -0.37 central slope value places this object in the weak cusp category.

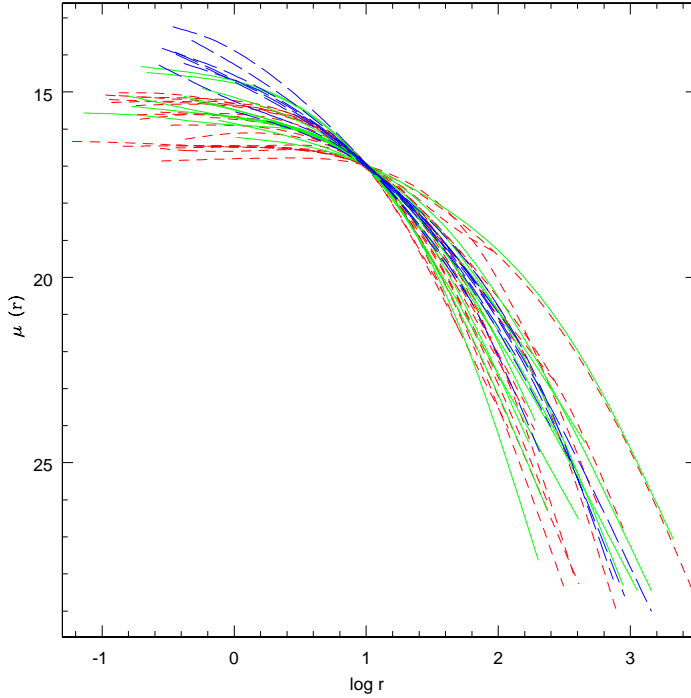


FIG. 13.— Surface brightness profiles for the entire sample. The profiles are normalized to a common point, therefore the units in the axis are arbitrary. Profiles are color coded according to their central slopes. Flat cores are shown in red (dashed lines), shallow cusps are shown in green (solid lines), and steep cusps are shown in blue (long dashed lines).

4.3.2. NGC 6535

NGC 6535 contains very few stars, therefore the image has low signal and the measured profile looks very noisy. We decided to include it in the sample because despite having so few stars, it shows a very steep central surface brightness profile. The photometric data shown in Trager’s catalog for this cluster shows an important deviation (~ 0.8 mag) with respect to the Chebychev polynomial fit between $2''$ and $15''$, where the photometric points are brighter than the polynomial fit. PSF effects might have been responsible for missing a cusp in this measurements.

4.3.3. NGC 6652

NGC 6652 is not considered to be in core collapse, but it shows a very concentrated profile in our measurements. Trager et al. (1995) report a $4''$ core for this object. Our power-law plus core fit finds a $1.15''$ core and it is consistent with the photometry within the error bars. This could be another case of a partially resolved core. The central slope from the smooth profile is -0.57 .

4.3.4. NGC 6752

NGC 6752 has been subject to a number of studies. This is the only cluster in our sample for which we only analyzed the PC chip, without including analysis of the WF chips. Lugger et al. (1995) analyzed a ground-based U-band image of the cluster and conclude that the surface brightness profile does not present a core-collapse morphology. Ferraro et al. (2003) constructed a surface density profile for this cluster based on star counts. They fit the central region with two separated King models, which they interpret as the cluster being in post-core-collapse bounce. Our results indicate a flat core

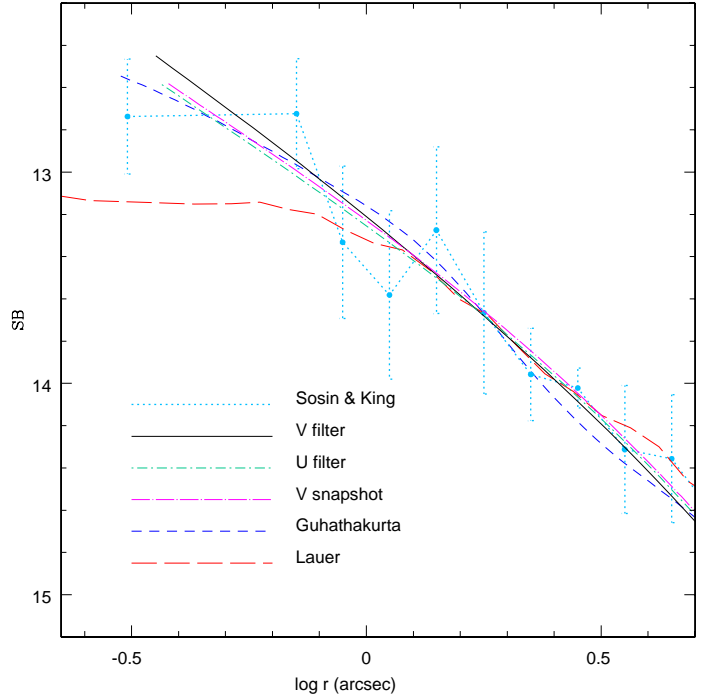


FIG. 14.— Surface brightness profiles for the central region of M15. Previously obtained profiles obtained by Guhathakurta (dashed dark blue), Sosin & King (dotted light blue) and Lauer et al. (long dashed red) are plotted with our results from various images: long exposure V image (solid black), long exposure U image (dotted -dashed green) and short exposure V (medium dashed magenta).

with a slope near zero for both the surface brightness and luminosity density profiles. Our difference from Ferraro et al. is likely due to noise in the star counts that they use.

4.3.5. M15

There are a variety of WFPC2 images available for M15. For this reason we applied the exact same procedure to each of them in order to test the reliability of the profiles. We have a high signal-to-noise F555 image, a F336 image and a snapshot (60 sec) F555 image. In Fig 14 we show our results for the inner part of the cluster, where we compare them with previously obtained profiles by Lauer et al. (1991), Guhathakurta et al. (1996) and Sosin & King (1997). Lauer et al’s analysis used a WFPC1 image, where they subtracted stars and measured the background starlight. Sosin & King’s curve comes from star counts in a narrow magnitude range and does not have any kind of smoothing applied to it, which is the reason why it looks much noisier than the other curves. Guhathakurta et al’s curve comes from corrected star counts and includes smoothing. All three curves have an arbitrary vertical scaling. It can be seen that the profiles are consistent in shape through this radial range (inner 5 arcseconds), with the exception of Lauer’s profile, which appears flat toward the center. The center we measure is within 0.1 from that obtained by both Guhathakurta and Sosin & King, so we are confident that center estimation is not a problem for this highly concentrated object.

When measuring logarithmic inner slopes, the choice of the radial extent used for the slope measurement is crucial. Sosin & King measure a -0.7 ± 0.5 logarithmic slope by fitting a power-law over a large radial extent between $0.3''$ and $10''$. Guhathakurta et al. report a slope of -0.82 ± 0.12 , again by

fitting a power-law between $0.3''$ and $6''$; this power-law fits the star counts near $6''$ but it is steeper than the points in the inner $0.5''$. We measure the slope only for the innermost points ($< 0.5''$) where it is a constant and get a value of -0.62 ± 0.06 . If the same procedure is applied to Guhathakurta et al.'s profile, we get a shallower slope of -0.46 .

5. SUMMARY

We obtain central surface brightness profiles for 38 galactic globular clusters from *HST*/WFPC2 images in various filters. Generally, we obtain reliable profiles into $0.5''$. Based on extensive simulations, we conclude that measuring integrated light with a robust statistical estimator is superior for estimation of the profiles as opposed to star counts when high signal to noise images are available. Profiles obtained from images taken with different filters are consistent and all are normalized to V-band by comparing to profiles from ground-based data.

When compared with previous ground based measurements, our profiles show different shapes for the inner regions. Most central surface brightness measured are brighter than previously reported with values up to two magnitudes brighter. The main reason for this difference is the increased spatial resolution of *HST*, but also because we use a non-parametric estimate as opposed to the traditional King model fits. The full distribution of central slopes is not consistent with simple isothermal cores. About half of our sample have a slope distribution consistent with King models (i.e. flat core) and our measurement uncertainties. The remaining 50%, however, have a distribution of SB logarithmic slopes that are fairly uniformly distributed from -0.2 to -0.8 . Our direct deprojection of the SB profiles produces similar results

for the luminosity density. About half of the sample have luminosity density logarithmic slopes that range from -0.4 to -1.7 .

We find it challenging to explain these slope distributions when we compare our results to existing dynamical models for globular clusters, such as core-collapse or those that include a central black hole. Both core-collapse and analytical black hole models predict luminosity density slopes around -1.6 . Core-collapse models can accommodate the cases of intermediate slopes (-0.2 to -0.5 in SB, and -0.2 to -1.3 in luminosity density) if we catch the clusters at the appropriate time, and it seems unlikely to find them in the high fraction that we measure. Recent numerical modeling for clusters containing black holes (Baumgardt et al. 2004) might be able to explain some of the intermediate slope cases.

Tables including our photometric measurements and fits can be found at:

www.as.utexas.edu/~eva/data.html.

This work is based in part on work supported by the Texas Advanced Research Program under grant 003658–0243–2001. We acknowledge the grant under HST-AR-09542 awarded by the Space Telescope Science Institute, which is operated by the Association of the Universities for Research in Astronomy, Inc., for NASA under contract NAS 5–26555. We also acknowledge the technical support from the Canadian Astronomy Data Centre, which is operated by the Herzberg Institute of Astrophysics, National Research Council of Canada. Finally, we acknowledge the support by CONACYT.

REFERENCES

- Bahcall, J. N., & Wolf, R. A. 1977, *ApJ*, 216, 883
 Bates, D., Lindstrom, M., Wahba, G., & Yandell, B. 1986, Technical Report 775, University of Wisconsin, Madison
 Baumgardt, H., Hegg, D. C., Hut, P., & Makino, J. 2003a, *MNRAS*, 341, 247
 Baumgardt, H., Hut, P., Makino, J., McMillan, S., & Portegies Zwart, S. 2003b, *ApJ*, 582, L21
 Baumgardt, H., Makino, J., & Ebisuzaki, T. 2004, *ApJL*, 613, 1143
 Beers, T. C., Flynn, K., & Gebhardt, K. 1990, *AJ*, 100, 32
 Breiden, J. L., Cohn, H. N., & Hut, P. 1994, *ApJ*, 421, 195
 Chernoff, D. F., & Weinberg, M. D. 1990, *ApJ*, 351, 121
 Cohn, H. 1980, *ApJ*, 242, 765
 Cohn, H., Hut, P., & Wise, M. 1989, *ApJ*, 342, 814
 Djorgovski, S. 1995, *ApJ*, 438, L29
 Djorgovski, S., & King, I. R. 1986, *ApJ*, 305, L61
 Dull, J. D., Cohn, H. N., Lugger, P. M., Murphy, B. W., Seitzer, P. O., Callanan, P. J., Rutten, R. G. M., & Charles, P. A. 1997, *ApJ*, 481, 267
 Ferraro, F. R., Possenti, A., Sabbi, E., Lagani, P., Rood, R. T., D'Amico, N., & Origlia, L. 2003, *ApJ*, 595, 179
 Gebhardt, K., Pryor, C., O'Connell, R. D., Williams, T. B., & Hesser, J. E. 2000, *AJ*, 119, 1268
 Gebhardt, K., Rich, R. M., & Ho, L. C. 2002, *ApJ*, 578, L41
 Gebhardt, K., et al. 1996, *AJ*, 112, 105
 Gerssen, J., van der Marel, R. P., Gebhardt, K., Guhathakurta, P., Peterson, R. C., & Pryor, C. 2002, *AJ*, 124, 3270
 Gerssen, J., van der Marel, R. P., Gebhardt, K., Guhathakurta, P., Peterson, R. C., & Pryor, C. 2003, *AJ*, 125, 376
 Gnedin, O. Y., Lee, H. M., & Ostriker, J. P. 1999, *ApJ*, 522, 935
 Grillmair, C. J., Freeman, K. C., Irwin, M., & Quinn, P. J. 1995, *AJ*, 109, 2553
 Guhathakurta, P., Webster, Z. T., Yanny, B., Schneider, D. P., & Bahcall, J. N. 1998, *AJ*, 116, 1757
 Guhathakurta, P., Yanny, B., Schneider, D. P., & Bahcall, J. N. 1996, *AJ*, 111, 267
 Harris, W. E. 1996, *AJ*, 112, 1487
 Howell, J. H., Guhathakurta, P., & Tan, A. 2000, *AJ*, 119, 1259
 Jimenez, R., & Padoan, P. 1998, *ApJ*, 498, 704
 King, I. R. 1966, *AJ*, 71, 276
 King, I. R., Sosin, C., & Cool, A. M. 1995, *ApJ*, 452, L33
 Lauer, T. R., et al. 1995, *AJ*, 110, 2622
 Lauer, T. R., et al. 2002, *AJ*, 124, 1975
 Lauer, T. R., et al. 1991, *ApJ*, 369, L45
 Lugger, P. M., Cohn, H. N., & Grindlay, J. E. 1995, *ApJ*, 439, 191
 Mackey, A. D., & Gilmore, G. F. 2003a, *MNRAS*, 338, 120
 Mackey, A. D., & Gilmore, G. F. 2003b, *MNRAS*, 338, 85
 Makino, J. 1996, *ApJ*, 471, 796
 Meylan, G., 191, 215
 Meylan, G., & Hegg, D. C., 8, 1
 Murphy, B. W., Cohn, H. N., & Hut, P. 1990, *MNRAS*, 245, 335
 Piotto, G., et al., 391, 945
 Silk, J., & Arons, J. 1975, *ApJ*, 200, L131
 Sosin, C. 1997, *AJ*, 114, 1517
 Sosin, C., & King, I. R. 1997, *AJ*, 113, 1328
 Stetson, P. B. 1987, *PASP*, 99, 191
 Trager, S. C., King, I. R., & Djorgovski, S. 1995, *AJ*, 109, 218
 Wahba, G. 1980, Technical Report 595, University of Wisconsin, Madison
 Wahba, G., & Wang, Y. 1990, *Communications in Statistics, Part A – Theory and Methods*, 19, 1685
 Yanny, B., Guhathakurta, P., Schneider, D. P., & Bahcall, J. N. 1994, *ApJ*, 435, L59

TABLE 1
SAMPLE.

NGC	other name	filter	exp. time	image name	α center	δ center
104	47Tuc	F555	723	u5470112b	00:24:05.47	-72:04:52.16
1851	...	F439	1200	u2va0103b	05:14:06.95	-40:02:44.61
1904	M79	F555	306	u3ki0201b	05:24:11.03	-24:31:29.50
2298	...	F814	905	u3kt010gb	06:48:59.44	-36:00:19.52
2808	...	F555	314	u4fp0105b	09:12:03.09	-64:51:48.96
5272	M3	F555	1260	u4r00101b	13:42:11.33	28:22:37.81
5286	...	F555	530	u3um0201b	13:46:26.73	-51:22:28.77
5694	...	F555	310	u2y70105b	14:39:36.29	-26:32:20.19
5824	...	F555	320	u2y70205b	15:03:58.63	-33:04:05.59
5897	...	F555	608	u3kt0204b	15:17:24.50	-21:00:37.00*
5904	M5	F336	1200	u3ki0302b	15:18:33.36	02:04:55.19
6093	M80	F675	780	u3mu0104b	16:17:02.48	-22:58:33.18
6205	M13	F555	2056	u5bt0104b	16:41:41.05	36:27:36.19
6254	M10	F336	1500	u3ki0102b	16:57:08.9	-09:05:58.0*
6266	M62	F555	562	u67e0209b	17:01:12.96	-30:06:46.20
6284	...	F555	164	u2xx0302b	17:04:28.51	-24:45:53.54
6287	...	F555	3160	u37a0106b	17:05:09.13	-22:42:30.14
6293	...	F555	202	u2xx0202b	17:10:10.31	-26:34:57.77
6341	M92	F555	428	u2z50109b	17:17:07.34	43:08:10.08
6333	M9	F555	2105	u28q0301b	17:19:11.26	-18:30:57.41
6352	...	F555	100	u2kl0205b	17:25:29.50	-48:25:19.65
6388	...	F336	1060	u63t0301b	17:36:17.18	-44:44:07.83
6397	...	F555	249	u33r010kb	17:40:41.57	-53:40:26.03
6441	...	F336	1060	u63t0401b	17:50:12.91	-37:03:06.67
6535	...	F555	1128	u3kt040gb	18:03:50.66	-00:17:53.03
6528	...	F555	814	u61v0101b	18:04:49.64	-30:03:22.55
6541	...	F555	596	u28q050hb	18:08:02.66	-43:42:52.92
6624	...	F555	1478	u28q0604b	18:23:40.22	-30:21:41.32
6626	M28	F555	1128	u3kt050gb	18:24:32.81	-24:52:11.20
6637	M69	F555	1690	u28q0704b	18:31:23.17	-32:20:54.59
6652	...	F555	1989	u3m8010ib	18:35:45.64	-32:59:26.99
6681	M70	F555	100	u24s0103t	18:43:12.83	-32:17:33.38
6712	...	F814	120	u2of0205t	18:53:04.30	-08:42:22.0*
6715	M54	F555	1850	u37ga40cb	18:55:03.29	-30:28:46.10
6752	...	F555	5246	u2hO010cb	19:10:52.237	-59:59:03.81
7078	M15	F555	400	u2hr0102b	21:29:58.40	12:10:00.26
7089	M2	F555	106	u67e0303b	21:33:27.00	-00:49:25.71
7099	M30	F555	1192	u5fw010nb	21:40:22.16	-23:10:47.64

TABLE 2
MEASURED PARAMETERS

NGC number	other name	$\mu_V(0)$ (mag/arcsec ²)	r_c (arcsec)	r_b (arcsec)	SB slope logarithmic	error	LD slope logarithmic	error
104	47Tuc	14.35	20.9	16.4	0.00	0.04	0.11	0.15
1851	...	13.30	2.0	4.6	-0.38	0.11	-1.03	0.11
1904	M79	15.67	5.6	14.8	-0.03	0.07	-0.01	0.39
2298	...	18.72	16.3	17.4	0.00	0.07	0.00	...
2808	...	14.89	12.4	36.1	-0.06	0.07	-0.66	0.54
5272	M3	15.72	14.6	46.9	-0.05	0.10	-0.39	0.45
5286	...	15.19	4.2	25.1	-0.28	0.11	-1.17	0.30
5694	...	15.62	2.2	2.6	-0.19	0.11	-0.73	0.41
5824	...	14.17	1.4	4.0	-0.36	0.16	-1.11	0.36
5897	...	20.47	84.9	119.0	-0.04	0.03	0.00	...
5904	M5	16.13	25.7	18.1	0.05	0.07	0.00	...
6093	M80	14.56	4.5	6.1	-0.16	0.07	-0.77	0.28
6205	M13	16.41	34.4	79.4	-0.10	0.15	-0.71	0.32
6254	M10	17.68	43.4	22.4	0.05	0.07	0.00	...
6266	M62	14.78	6.6	13.8	-0.13	0.08	-0.74	0.40
6284	...	14.66	1.1	...	-0.55	0.14	-1.39	0.19
6287	...	18.32	11.3	34.4	0.00	0.07	-0.04	0.30
6293	...	14.43	1.0	...	-0.67	0.08	-1.27	0.18
6341	M92	15.29	11.0	17.15	-0.01	0.04	0.00	...
6333	M9	17.01	19.1	41.8	0.00	0.13	0.00	...
6352	...	18.31	23.2	24.0	0.02	0.17	0.00	...
6388	...	14.68	4.4	5.0	-0.13	0.07	-0.57	0.21
6397	...	15.29	3.7	2.7	-0.37	0.11	-1.16	0.20
6441	...	14.76	5.8	12.6	-0.02	0.12	-0.02	0.35
6535	...	19.35	1.7	21.2	-0.50	0.18	-1.28	0.38
6528	...	16.56	3.9	6.7	-0.10	0.14	-0.23	0.29
6541	...	14.38	2.0	...	-0.41	0.09	-1.32	0.22
6624	...	14.35	1.7	4.28	-0.32	0.16	-1.15	0.31
6626	M28	15.55	9.8	8.9	0.03	0.05	0.00	...
6637	M69	16.71	16.4	49.5	0.09	0.13	0.00	...
6652	...	13.93	1.2	0.7	-0.57	0.12	-1.44	0.20
6681	M70	13.68	1.1	...	-0.82	0.09	-1.75	0.10
6712	...	18.57	37.3	68.6	0.02	0.05	0.00	...
6715	M54	14.12	3.2	8.2	-0.12	0.07	-0.71	0.35
6752	...	14.56	6.53	3.2	-0.03	0.15	0.00	...
7078	M15	12.45	0.98	...	-0.66	0.11	-1.56	0.22
7089	M2	15.19	12.9	20.8	0.05	0.11	0.00	...
7099	M30	14.22	1.6	...	-0.57	0.11	-1.42	0.18

NOTE. — col 1-2 are NGC and other names, col 3 is central surface brightness in V, col 4 is core radius, col 5 is break radius (as defined on Section 3.2), col 6-7 are logarithmic central surface brightness slope and uncertainty, col 8-9 are logarithmic central luminosity density slope and uncertainty.